

See discussions, stats, and author profiles for this publication at: <https://www.researchgate.net/publication/355698722>

On Computing the Hyperparameter of Extreme Learning Machines: Algorithm and Application to Computational PDEs, and Comparison with Classical and High-Order Finite Elements

Preprint · October 2021

CITATIONS

0

READS

19

2 authors, including:



[Steven Dong](#)

Purdue University

106 PUBLICATIONS 2,442 CITATIONS

SEE PROFILE

On Computing the Hyperparameter of Extreme Learning Machines: Algorithm and Application to Computational PDEs, and Comparison with Classical and High-Order Finite Elements

Suchuan Dong*, Jielin Yang
Center for Computational and Applied Mathematics
Department of Mathematics
Purdue University, USA

(October 26, 2021)

Abstract

We consider the use of extreme learning machines (ELM) for computational partial differential equations (PDE). In ELM the hidden-layer coefficients in the neural network are assigned to random values generated on $[-R_m, R_m]$ and fixed, where R_m is a user-provided constant, and the output-layer coefficients are trained by a linear or nonlinear least squares computation. We present a method for computing the optimal or near-optimal value of R_m based on the differential evolution algorithm. This method seeks the optimal R_m by minimizing the residual norm of the linear or nonlinear algebraic system that results from the ELM representation of the PDE solution and that corresponds to the ELM least squares solution to the system. It amounts to a pre-processing procedure that determines a near-optimal R_m , which can be used in ELM for solving linear or nonlinear PDEs. The presented method enables us to illuminate the characteristics of the optimal R_m for two types of ELM configurations: (i) Single-Rm-ELM, corresponding to the conventional ELM method in which a single R_m is used for generating the random coefficients in all the hidden layers, and (ii) Multi-Rm-ELM, corresponding to a modified ELM method in which multiple R_m constants are involved with each used for generating the random coefficients of a different hidden layer. We adopt the optimal R_m from this method and also incorporate other improvements into the ELM implementation. In particular, here we compute all the differential operators involving the output fields of the last hidden layer by a forward-mode auto-differentiation, as opposed to the reverse-mode auto-differentiation in a previous work. These improvements significantly reduce the network training time and enhance the ELM performance. We systematically compare the computational performance of the current improved ELM with that of the finite element method (FEM), both the classical second-order FEM and the high-order FEM with Lagrange elements of higher degrees, for solving a number of linear and nonlinear PDEs. It is shown that the current improved ELM far outperforms the classical FEM. Its computational performance is comparable to that of the high-order FEM for smaller problem sizes, and for larger problem sizes the ELM markedly outperforms the high-order FEM.

Keywords: *extreme learning machine, local extream learning machine, neural network, least squares, nonlinear least squares, differential evolution*

Contents

1	Introduction	2
2	Computing the Optimal R_m Constant(s) in ELM	4
2.1	The Maximum Magnitude of Random Coefficients (R_m)	4
2.2	ELM Configuration with a Single R_m Constant (Single-Rm-ELM)	5
2.3	ELM Configuration with Multiple R_m Constants (Multi-Rm-ELM)	9

*Author of correspondence. Email: sdong@purdue.edu

3	Numerical Examples	11
3.1	General Notes on the Implementations	11
3.2	Function Approximation	13
3.3	Poisson Equation	18
3.4	Nonlinear Helmholtz Equation	26
3.5	Viscous Burgers' Equation	33
4	Concluding Remarks	41

1 Introduction

This work focuses on the use of extreme learning machines (ELM) for computational partial differential equations (PDE). ELM was originally developed in [26, 27] for linear classification/regression problems with single hidden-layer feed-forward neural networks, and has since found wide applications in a number of fields; see the reviews in [25, 1] and the references therein. Two strategies underlie ELM: (i) random but fixed (non-trainable) hidden-layer coefficients, and (ii) trainable linear output-layer coefficients determined by a linear least squares method or by using the pseudo-inverse of the coefficient matrix (for linear problems). The ELM type idea has also been developed for nonlinear problems; see e.g. [10, 11] for solving stationary and time-dependent nonlinear PDEs in which the neural network is trained by a nonlinear least squares method. Following [11], we broadly refer to the artificial neural network-based methods exploiting these strategies as ELM type methods, including those employing neural networks with multiple hidden layers and those for nonlinear problems [49, 51, 10, 11, 17].

Our research is motivated by the following questions:

- Can artificial neural networks provide a competitive technique for scientific computing and in particular for computational PDEs?
- Can we devise a neural network-based method for approximating PDEs that can outcompete traditional numerical techniques in computational performance?

These questions have been hanging in the air ever since the early studies on neural networks for differential equations in the 1990s (see e.g. [35, 39, 40, 58, 33]). The remarkable success of deep learning [20] in the last decade or so has stimulated a significant amount of efforts in the development of deep neural network (DNN) based PDE solvers and scientific machine learning [29, 46, 42, 15, 52]. By exploiting the universal approximation property of neural networks [23, 24, 5, 37], these solvers transform the PDE solution problem into an optimization problem. The field function is represented by a neural network, whose weight/bias coefficients are adjusted to minimize an appropriate loss function. The differential equation, the boundary and initial conditions are then encoded into the loss function by penalizing some residual norms of these quantities in strong or weak forms [33, 34, 46, 42, 15, 60, 32]. The differential operators involved therein are usually computed analytically with shallow neural networks in the early works (see e.g. [33]), and in modern implementations they are typically computed by auto-differentiation [2] available from the common machine learning libraries such as Tensorflow (www.tensorflow.org) and PyTorch (pytorch.org). The minimization of the loss function is performed by an optimizer, which is usually based on some flavor of gradient descent or back propagation type techniques [55, 21]. The optimization process constitutes the predominant computations in the neural network-based PDE solvers, and it is commonly known as the training of the neural network. Upon convergence of the optimization process, the PDE solution is given by the neural network, with the adjustable weight/bias parameters set based on their converged values. A number of prominent works on DNN-based PDE solvers have appeared in the literature, and we refer the reader to e.g. [42, 46, 15, 43, 56, 22, 31, 60, 54, 44, 36, 28, 50, 3, 53, 12] (among others), and also the review article [29] and the references contained therein.

As discussed in [10], while their computational performance is promising, the existing DNN-based PDE solvers suffer from several drawbacks: limited accuracy, general lack of convergence with a certain convergence rate, and extremely high computational cost (very long time to train). We refer the reader to [10] for more detailed discussions of these aspects. These drawbacks make such solvers numerically less than attractive and computationally uncompetitive. There is mounting evidence that these solvers, in their current state, seem to

fall short and cannot compete with traditional numerical methods for commonly-encountered computational PDE problems (especially in low dimensions) [10].

The pursuit for higher accuracy and more competitive performance with neural networks for computational PDEs has led us in [10, 11] to explore randomized neural networks (including ELM) [45, 18]. Since optimizing the entire set of weight/bias coefficients in the neural network can be extremely hard and costly, perhaps randomly assigning and fixing a subset of the network’s weights will make the resultant optimization task of network training simpler, and ideally linear, without severely sacrificing the achievable approximation capacity. This is the basic strategy in randomizing the neural networks. In ELM one assigns random values to and fixes the hidden-layer coefficients, and only allows the output-layer (assumed to be linear) coefficients to be trainable. For linear problems, the resultant system becomes linear with respect to the output-layer coefficients, which can then be determined by a linear least squares method [26, 41, 14, 10, 11, 4]. Random-weight neural networks similarly possess a universal approximation property. It has been shown in [27] that a single hidden-layer feed-forward neural network having random but fixed (not trained) hidden nodes can approximate any continuous function to any desired degree of accuracy, provided that the number of hidden units is sufficiently large.

In [10] we have developed a local version of the ELM method (termed locELM) for solving linear and nonlinear PDEs, which combines the ideas of ELM, domain decomposition, and local neural networks. We use a local feed-forward neural network to represent the field solution on each sub-domain, and impose C^k (with an appropriate k) continuity conditions on the sub-domain boundaries. The weight/bias coefficients in all the hidden layers of the local neural networks are preset to random values generated on $[-R_m, R_m]$ (R_m denoting a user-provided constant) and fixed, and the weights of the linear output layers of the local networks are trained by a linear least squares method for linear PDEs or by a nonlinear least squares method for nonlinear PDEs. For time-dependent linear/nonlinear PDEs, we have introduced a block time marching scheme together with locELM for long-time dynamic simulations. Note that locELM reduces to (global) ELM if a single subdomain is used in the domain decomposition. Most interesting is that locELM is highly accurate and computationally fast. This method exhibits a clear sense of convergence with respect to the degrees of freedom in the neural network. For smooth PDE solutions, its numerical errors decrease exponentially or nearly exponentially as the number of training parameters or the number of training data points increases, reminiscent of the spectral convergence of traditional high-order methods such as the spectral, spectral element or hp-finite element (high-order finite element) type techniques [30, 48, 61, 59, 13, 8, 7, 38, 57]. When the number of degrees of freedom (number of training collocation points, number of training parameters) becomes large, the errors of locELM can reach a level close to the machine zero.

More importantly, it is shown in [10] that the computational performance (accuracy, computational cost) of locELM is on par with that of the classical FEM (2nd order, linear elements), and locELM outperforms the classical FEM for larger problem sizes. Here for locELM the computational cost refers to the time for training the neural network and related computations, and for FEM it refers to the FEM computation time (see [10] for details). By “outperform” we mean that one method achieves a better accuracy under the same computational budget/cost or incurs a lower computational cost to achieve the same accuracy. More specifically, there is a cross-over point in the relative performance between locELM and the FEM with respect to the problem size. The classical FEM typically outperforms locELM for smaller problem sizes, and for larger problem sizes locELM outperforms the classical FEM [10].

Some comparisons between locELM and the high-order FEM (employing high-order Lagrange elements) for the 2D Poisson equation have also been conducted in [10]. It is observed that the locELM method can outperform the Lagrange elements of degree 2, but can barely outperform the Lagrange elements of degree 3. The method as implemented in [10] cannot outcompete high-order FEM with element degrees 4 or larger. Overall the method of [10] seems competitive to some degree when compared with the high-order FEM, but it is in general not as efficient as the latter as of the writing of [10]. This inefficiency in comparison with high-order FEM is the primary motivator for the current work.

We would like to mention that in [10] a systematic comparison between locELM and two state-of-the-art DNN-based PDE solvers, the deep Galerkin method (DGM) [46] and the physics-informed neural network (PINN) method [42], has also been performed. It is shown that locELM outperforms PINN and DGM by a considerable degree. The numerical errors and the computational cost (network training time) of locELM are considerably smaller, typically by orders of magnitude, than those of DGM and PINN.

In the current paper we present improvements to the ELM technique (which also apply to locELM) in two

aspects. First, we present a method for computing the optimal (or near-optimal) value of the R_m constant in ELM, i.e. the maximum magnitude of the random hidden-layer coefficients. Note that in [10] R_m is estimated by using a preliminary simulation with manufactured solutions for a given problem. The method presented here is based on the differential evolution algorithm [47], and seeks the optimal R_m by minimizing the residual norm of the linear/nonlinear algebraic system that results from the ELM representation of the PDE solution and that corresponds to the ELM least squares solution to the system. This method amounts to a pre-processing procedure that determines a near-optimal value for R_m , which can be used in ELM for solving linear or nonlinear PDEs.

The procedure for computing the optimal R_m enables us to investigate two types of ELM methods based on how the random hidden-layer coefficients are assigned: Single-Rm-ELM and Multi-Rm-ELM. The Single-Rm-ELM configuration corresponds to the conventional ELM method, in which the weight/bias coefficients in all the hidden layers are set to random values generated on $[-R_m, R_m]$, with a single R_m for all hidden layers. The Multi-Rm-ELM configuration corresponds to a modified ELM method, in which the weight/bias coefficients for any given hidden layer are set to random values generated on $[-R_m, R_m]$, with a different R_m value for a different hidden layer. Therefore, multiple R_m constants are involved in Multiple-Rm-ELM for assigning the random coefficients, with each corresponding to a different hidden layer. The characteristics of the optimal R_m corresponding to these two types of ELM configurations are studied and illuminated. The Multi-Rm-ELM configuration leads to more accurate simulation results than Single-Rm-ELM.

The second aspect of improvement is in the implementation of the ELM method. A major change in the current work lies in that here we compute all the differential operators involving the output fields of the last hidden layer of the neural network by the forward-mode auto-differentiation, implemented by the “ForwardAccumulator” in the Tensorflow library. In contrast, in the ELM implementation of [10] these differential operators are computed by the default reverse-mode auto-differentiation (“GradientTape”) in Tensorflow. Because in ELM the number of nodes in the last hidden layer is typically much larger than that of the input layer, this change reduces the ELM network training time dramatically.

Building upon these improvements, in the current paper we systematically compare the current improved ELM with the classical FEM (2nd-order) and the high-order FEM employing Lagrange elements of higher degrees (with both h-type and p-type refinements) for solving a number of linear and nonlinear PDEs. We show that the improved ELM far outperforms the classical FEM. The ELM’s computational performance is comparable to that of the high-order FEM for smaller problem sizes, and for larger problem sizes the ELM markedly outperforms the high-order FEM. Overall, the current ELM method is computationally far more competitive than the classical FEM, and is more competitive than or as competitive as the high-order FEM.

As in [10], the ELM method here is implemented in Python using the Tensorflow and Keras (keras.io) libraries. The classical FEM and the high-order FEM are implemented in Python using the FEniCS library, in which the linear and higher-order Lagrange elements are available.

The rest of this paper is structured as follows. In Section 2 we present the method for computing the optimal R_m constant(s) with the Single-Rm-ELM and Multi-Rm-ELM configurations based on the differential evolution algorithm. In Section 3 we investigate the characteristics of the optimal R_m and study the effect of the network/simulation parameters on the optimal R_m for function approximation and for solving linear/nonlinear PDEs. We compare systematically the computational performance of the ELM and the classical/high-order FEMs for solving the differential equations. In Section 4 we summarize the common characteristics of the optimal R_m in Single-Rm-ELM and Multi-Rm-ELM and also the performance comparisons between ELM and classical/high-order FEM to conclude the presentations.

2 Computing the Optimal R_m Constant(s) in ELM

2.1 The Maximum Magnitude of Random Coefficients (R_m)

When the ELM method is used to solve linear/nonlinear PDEs, the hidden-layer coefficients are set to uniform random values generated on the interval $[-R_m, R_m]$, where R_m is a user-defined constant (see [10, 11]). The R_m constant is a hyperparameter of the ELM method. Its value can have a marked influence on the accuracy of the ELM results [10]. The best accuracy is typically associated with R_m from a range of moderate values, while very large or very small R_m values can result in simulation results with poor or

poorer accuracy (see [10] for details). For a given problem, in [10] the R_m (or the optimal range of R_m) is estimated by preliminary simulations using some manufactured solution.

One goal of this work is to devise a method to attain the optimal or near-optimal value of the constant R_m for a given problem. This method enables us to explore and study the characteristics of and the effects of the simulation/network parameters on the optimal R_m . In particular, it enables us to look into a modified ELM method, which employs multiple R_m constants, each for generating the random coefficients of a different hidden layer, in a deeper neural network. The use of multiple R_m constants in ELM leads to more accurate simulation results. It would be extremely difficult, and often practically impossible, to determine an optimal vector of R_m values without the automatic procedure.

The method for computing the optimal R_m presented here amounts to a pre-processing procedure. It only needs to be performed when a given problem (or some configuration) is considered for the first time. The R_m in ELM can then be fixed to the value obtained by the method in subsequent computations. As will become clear in later sections, the optimal R_m is insensitive to the number of training collocation points and has a quite weak dependence on the number of training parameters. In addition, the R_m values in a range around the optimal R_m lead to comparable and essentially the same accuracy as the optimal R_m . Therefore, for a given problem one can basically employ a specific set of collocation points and a specific number of training parameters to compute the optimal R_m using the method developed here. Then in subsequent computations one can fix the R_m in ELM at the returned value for a different set of collocation points or different number of training parameters. This is especially useful in long-time dynamic simulations of time-dependent PDEs by the block time marching scheme [10]. The pre-processing computation for the optimal R_m only needs to be performed using the spatial-temporal domain of the first time block. Then the R_m fixed at the returned value can be used for ELM computations on all the time blocks.

2.2 ELM Configuration with a Single R_m Constant (Single-Rm-ELM)

We now develop a procedure for computing the optimal R_m constant in ELM for solving partial differential equations. Consider a domain Ω in d ($d = 1, 2$ or 3) dimensions, and the following generic boundary value problem on Ω ,

$$\mathbf{L}(\mathbf{u}) = \mathbf{f}(\mathbf{x}), \quad (1a)$$

$$\mathbf{B}(\mathbf{u}) = \mathbf{g}(\mathbf{x}), \quad \text{on } \partial\Omega, \quad (1b)$$

where \mathbf{L} and \mathbf{B} are differential (or algebraic) operators that may be linear or nonlinear, $\mathbf{u}(\mathbf{x})$ is the field function to be solved for, \mathbf{f} and \mathbf{g} are given functions (source terms) in the domain Ω or on the domain boundary $\partial\Omega$. We assume that this problem is well-posed.

We solve this problem using a feed-forward neural network by the ELM method (see [10]). Let the vector $[M_0, M_1, \dots, M_L]$ denote the architecture of the neural network, where $(L+1)$ is the number of layers in the neural network with $L \geq 2$, and $M_i \geq 1$ denotes the number of nodes in layer i ($0 \leq i \leq L$). The input layer (i.e. layer 0) to the neural network represents the coordinate \mathbf{x} , with $M_0 = d$. The output layer (i.e. layer L) represents the field solution $\mathbf{u}(\mathbf{x})$, with M_L being the dimension of \mathbf{u} . Those layers in between are the hidden layers.

The neural network logically represents a parameterized function constructed through repeated function compositions with a nonlinear activation function and repeated affine transforms [20]. More specifically, we choose a set of Q discrete points (collocation points) on the domain Ω , among which Q_b ($1 \leq Q_b < Q$) points reside on the boundary $\partial\Omega$, and these are the training data points. We use

$$Z = \{\mathbf{x}_i \in \Omega, \ 1 \leq i \leq Q\}, \quad \text{and } Z_b = \{\mathbf{x}_i \in Z \text{ and } \mathbf{x}_i \in \partial\Omega, \ 1 \leq i \leq Q_b\} \quad (2)$$

to denote the set of all collocation points and set of boundary collocation points, respectively. Let the matrix \mathbf{X} of dimension $Q \times M_0$ denote the coordinates of the collocation points, which are the input data to the network. Let the matrix \mathbf{U} of dimension $Q \times M_L$ denote the output data of the neural network, which represent $\mathbf{u}(\mathbf{x})$ on the collocation points. Let the matrix Φ_l of dimension $Q \times M_l$ denote the output data of layer l ($0 \leq l \leq L$), with $\Phi_0 = \mathbf{X}$ and $\Phi_L = \mathbf{U}$. Then the logic of the hidden layer l ($1 \leq l \leq L-1$) is represented by

$$\Phi_l = \sigma(\Phi_{l-1}\mathbf{W}_l + \mathbf{b}_l), \quad 1 \leq l \leq L-1, \quad (3)$$

where $\sigma(\cdot)$ is the activation function, \mathbf{W}_l is a constant matrix of dimension $M_{l-1} \times M_l$ representing the weight coefficients of layer l , and \mathbf{b}_l is a row vector of dimension $1 \times M_l$ representing the biases of this layer. Note that we have used the convention (as in the Python language) here that when computing the right hand side of (3) the data in \mathbf{b}_l will be propagated along the first dimension to form a $Q \times M_l$ matrix.

With the ELM method, we follow [10] to set the weight/bias coefficients in all the hidden layers, $(\mathbf{W}_l, \mathbf{b}_l)$ for $1 \leq l \leq L-1$, to uniform random values generated on $[-R_m, R_m]$, and fix their values (not trainable) once they are set. The output layer is required to be linear, i.e. without the activation function, with zero bias. The logic of the output layer is given by,

$$\mathbf{U} = \Phi_{L-1} \mathbf{W}_L \quad (4)$$

where \mathbf{W}_L is a $M_{L-1} \times M_L$ constant matrix denoting the weights of the output layer, which are the trainable parameters of the ELM neural network.

On the continuum level, the relation (4) becomes the following in terms of the coordinate \mathbf{x} ,

$$u_i(\mathbf{x}) = \sum_{j=1}^M V_j(\mathbf{x}) \beta_{ji}, \quad 1 \leq i \leq M_L, \quad (5)$$

where $\mathbf{u} = (u_1, u_2, \dots, u_{M_L})$, $\mathbf{W}_L = [\beta_{ij}]_{M_{L-1} \times M_L}$, and $M = M_{L-1}$ denotes the number of nodes in the last hidden layer, which can be large in the ELM neural network. $V_j(\mathbf{x})$ ($1 \leq j \leq M$) are the output fields of the last hidden layer, whose data on the collocation points are given by Φ_{L-1} .

Substituting the expression (5) for $\mathbf{u}(\mathbf{x})$ into the system (1), enforcing (1a) on all the collocation points in Z and enforcing (1b) on all the boundary collocation points in Z_b , we have

$$\mathbf{L} \left(\sum_{j=1}^M V_j(\mathbf{x}_p) \beta_j \right) = \mathbf{f}(\mathbf{x}_p), \quad \text{for all } \mathbf{x}_p \in Z, \quad 1 \leq p \leq Q, \quad (6a)$$

$$\mathbf{B} \left(\sum_{j=1}^M V_j(\mathbf{x}_q) \beta_j \right) = \mathbf{g}(\mathbf{x}_q), \quad \text{for all } \mathbf{x}_q \in Z_b, \quad 1 \leq q \leq Q_b, \quad (6b)$$

where $\beta_j = (\beta_{j1}, \beta_{j2}, \dots, \beta_{jM_L})$. This is a system of $(Q + Q_b)$ algebraic equations about the training parameters $\mathbf{W}_L = [\beta_{ij}]_{M_{L-1} \times M_L}$. This system is linear with respect to β_{ij} if the original system (1) is linear with respect to \mathbf{u} , and it is nonlinear if the original system (1) is nonlinear. Following [10], we solve this algebraic system (6) for β_{ij} by the linear least squares (LLSQ) method if it is linear, and by the nonlinear least squares method with perturbations (NLLSQ-perturb) if it is nonlinear; see [10] for details.

What has been discussed so far is the main idea of the ELM method from [10] for solving the system (1). Let us now consider how to determine the optimal value for the R_m constant.

We first modify the generation of the random hidden-layer coefficients as follows. Let $N_h = \sum_{l=1}^{L-1} (M_{l-1} + 1) M_l$ denote the total number of hidden-layer coefficients (weights/biases) in the neural network. We first generate a set of N_h uniform random values on the interval $[-1, 1]$, which will be denoted by the vector $\boldsymbol{\xi}$ of length N_h . Once $\boldsymbol{\xi}$ is generated, it will be fixed throughout the computation. Given a constant R_m , the vector $R_m \boldsymbol{\xi}$ contains a set of N_h random values on $[-R_m, R_m]$, and we will set the random hidden-layer coefficients, $(\mathbf{W}_l, \mathbf{b}_l)$ for $1 \leq l \leq L-1$, by the random vector $R_m \boldsymbol{\xi}$. With this modification the R_m constant becomes a scaling coefficient, and it is not confined to positive values. In the following discussions R_m can in principle assume positive, zero, or negative values.

Let β_{ij}^{LS} ($1 \leq i \leq M_{L-1}$, $1 \leq j \leq M_L$) denote the least squares solution to the system (6) obtained by the linear or nonlinear least squares method. Define the residual vector \mathbf{r} , with length $(Q + Q_b)$, of the

Algorithm 1: Computing the cost function $\mathcal{N}(R_m)$ in Single-Rm-ELM

input : R_m ; input data \mathbf{X} to neural network; fixed random vector $\boldsymbol{\xi}$, of length N_h containing uniform random values on $[-1, 1]$.

output: $\mathcal{N}(R_m)$.

- 1 update the hidden-layer coefficients, $(\mathbf{W}_l, \mathbf{b}_l)$ for $1 \leq l \leq L-1$, by $R_m \boldsymbol{\xi}$
 - 2 compute Φ_{L-1} by evaluating the neural network (first $(L-1)$ layers) on the input data \mathbf{X}
 - 3 solve system (6) for β_{ij}^{LS} by the linear or nonlinear least squares method from [10]
 - 4 update the output-layer coefficients \mathbf{W}_L by β_{ij}^{LS} ($1 \leq i \leq M_{L-1}$, $1 \leq j \leq M_L$)
 - 5 compute \mathbf{u}^{LS} , $\mathbf{L}(\mathbf{u}^{LS})$ and $\mathbf{B}(\mathbf{u}^{LS})$ by evaluating the neural network on \mathbf{X} and by auto-differentiation
 - 6 compute the residual vector $\mathbf{r}(R_m)$ by equation (7)
 - 7 compute $\mathcal{N}(R_m)$ by equation (8)
-

system (6) at the least squares solution,

$$\mathbf{r}(R_m) = \begin{bmatrix} \vdots \\ \mathbf{L} \left(\sum_{j=1}^M V_j(\mathbf{x}_p, R_m) \beta_j^{LS} \right) - \mathbf{f}(\mathbf{x}_p) \\ \vdots \\ \vdots \\ \mathbf{B} \left(\sum_{j=1}^M V_j(\mathbf{x}_q, R_m) \beta_j^{LS} \right) - \mathbf{g}(\mathbf{x}_q) \\ \vdots \end{bmatrix} = \begin{bmatrix} \vdots \\ \mathbf{L}(\mathbf{u}^{LS}(\mathbf{x}_p, R_m)) - \mathbf{f}(\mathbf{x}_p) \\ \vdots \\ \vdots \\ \mathbf{B}(\mathbf{u}^{LS}(\mathbf{x}_q, R_m)) - \mathbf{g}(\mathbf{x}_q) \\ \vdots \end{bmatrix} \quad (7)$$

where $\beta_j^{LS} = (\beta_{j1}^{LS}, \beta_{j2}^{LS}, \dots, \beta_{jM_L}^{LS})$, $\mathbf{u}^{LS} = \sum_{j=1}^M V_j \beta_j^{LS}$ is the least squares solution, $\mathbf{x}_p \in Z$ and $\mathbf{x}_q \in Z_b$. Note that here the dependence of the residual $\mathbf{r}(R_m)$, the output fields of the last hidden layer $V_j(\mathbf{x}, R_m)$, and the least squares solution $\mathbf{u}^{LS}(\mathbf{x}, R_m)$ on the scaling coefficient R_m has been made explicit. Let

$$\mathcal{N}(R_m) = \|\mathbf{r}(R_m)\| \quad (8)$$

denote the Euclidean norm of the residual vector $\mathbf{r}(R_m)$.

We seek the optimal value R_{m0} for R_m such that the norm $\mathcal{N}(R_m)$ is minimized, i.e.

$$R_{m0} = \arg \min_{R_m} \mathcal{N}(R_m). \quad (9)$$

This is an optimization problem of a scalar function with a single variable. Note that the derivative $\mathcal{N}'(R_m)$ may be approximated by finite difference. But in general $\mathcal{N}'(R_m)$ cannot be computed directly based on the system (6), if this system is nonlinear. This is because of the nonlinear least squares solution β_{ij}^{LS} involved therein. If this system is linear $\mathcal{N}'(R_m)$ can be computed from (6) in principle.

A number of methods can be used for solving the problem (9). In the current work we adopt the differential evolution (DE) algorithm [47] for computing R_{m0} . Differential evolution is a population-based evolutionary (genetic) algorithm for continuous functions. The implementation of differential evolution is available in several scientific libraries, e.g. the Tensorflow-Probability library (www.tensorflow.org/probability) and the scipy library. In the current paper we employ the scipy implementation for the differential evolution algorithm. This algorithm requires, as an input argument, a routine for evaluating the cost function $\mathcal{N}(R_m)$ for any given R_m . The procedure for computing $\mathcal{N}(R_m)$ is summarized in Algorithm 1.

Remark 2.1. If the system (6) is linear, then in line 2 of the Algorithm 1 one also needs to compute the derivatives of Φ_{L-1} involved in the $\mathbf{L}(\mathbf{u})$ and $\mathbf{B}(\mathbf{u})$ operators. This can be done by auto-differentiation. In this case, in line 5 of Algorithm 1, one can compute \mathbf{u}^{LS} by equation (4), and compute $\mathbf{L}(\mathbf{u}^{LS})$ and $\mathbf{B}(\mathbf{u}^{LS})$ by multiplying \mathbf{W}_L to the appropriate derivatives already computed in line 2.

When solving a linear system (6), it is important to avoid implementations of linear least squares solvers employing normal equations (e.g. the Tensorflow’s “lstsq” routine with the default “fast” option), which can lead to severe ill-conditioning and significantly lower accuracy, even if the original system is only moderately ill-conditioned [19]. In the current paper (and in [10]), we employ the linear least squares routine from the LAPACK, available through the wrapper function in the scipy package (“scipy.linalg.lstsq”).

Remark 2.2. The computation for R_{m0} amounts to a pre-processing procedure, which can be performed when a given problem setting or neural network setup is considered for the first time. In subsequent computations the R_m in ELM can be fixed to the attained R_{m0} (or a value nearby). Numerical experiments indicate that the optimal R_m in Single-Rm-ELM is not sensitive to the number of collocation points and only weakly depends on the number of training parameters, and that the R_m values in a range around the optimum R_{m0} lead to essentially the same accuracy as R_{m0} . Therefore, in general one can use a specific set of degrees of freedom (number of collocation points and training parameters) in the pre-processing run to compute the optimal R_m . Then the R_m fixed at the obtained value can be used in subsequent computations with other sets degrees of freedom or simulation parameters. Oftentimes one would like to perform a series of simulations with a simulation parameter varied in a range of values, e.g. varying the number of training parameters between 10 and 500. In this case, one can compute the R_{m0} in the pre-processing run with a representative value for this parameter. One can typically use a larger value (e.g. the largest or close to the largest value) for this simulation parameter. The resultant R_{m0} can be used for R_m to perform the planned series of simulations.

When computing the R_{m0} during pre-processing we require that the number of collocation points be sufficiently large such that in the system (6) the number of equations is larger than the number of unknowns. This is to try to avoid the regime where, if the system is linear, its coefficient matrix may become rank deficient.

Remark 2.3. The methods for computing the optimal R_m and for solving PDEs using ELM all involve random number generators. Given a specific problem to be solved, in the current work we require that the seed for the random number generator be fixed when computing the R_{m0} during pre-processing and when using the ELM with a fixed R_m to solve the PDE subsequently. In other words, the random number generator should be initialized by the same fixed seed in all these computations. The specific seed value is unimportant, as long as the random numbers are all generated by that seed. This is to ensure that the random coefficients of the neural network in the pre-processing run for computing the R_{m0} , and in the subsequent ELM runs using the attained R_{m0} value, are generated by the same seed. A fixed and known seed value also makes all the ELM simulation results (their numerical values) deterministic and exactly reproducible. We follow this convention in all the numerical experiments reported in Section 3.

Remark 2.4. In addition to differential evolution, we have also considered the simplicial homology global optimization (SHGO) algorithm [16] (implementation also available from scipy) for computing the R_{m0} . The results from SHGO and from differential evolution are comparable. We only consider the results from the differential evolution algorithm in Section 3. When one uses the differential evolution implementation from scipy a pair of values, (R_{\min}, R_{\max}) , needs to be provided to serve as the lower/upper bounds for the range of R_m values.

Remark 2.5. One should note that the computed R_{m0} is but a reference value in practice. The R_m values in a neighborhood of R_{m0} typically lead to simulation results with comparable or essentially the same accuracy. Therefore, in ELM simulations one can usually employ a “nicer” R_m value that is close to R_{m0} , instead of R_{m0} itself. For example, with an $R_{m0} = 1.24931$ obtained from the method, one can typically employ $R_m = 1.25$ in subsequent ELM computations to attain results with the same or similar accuracy.

Remark 2.6. For a nonlinear system (6), when computing R_{m0} one can turn off the initial-guess perturbations and the associated sub-iterations in the NLLSQ-perturb method (see [10] for details). In other words, in the R_{m0} computation we can solve the nonlinear algebraic system (6) for β_{ij} using the nonlinear least squares method without perturbations. This is because only the relative merits of different R_m values are important when computing the optimal R_m . Once the R_{m0} is obtained, one can turn on the perturbations in the subsequent ELM computations with the NLLSQ-perturb method.

Remark 2.7. If the PDE is time-dependent and the temporal domain $[0, T]$ is small, we can treat the time variable t in the same way as the spatial coordinate \mathbf{x} , e.g. by treating t as the $(d+1)$ -th independent variable,

and generate collocation points in the spatial-temporal domain $\Omega \times [0, T]$. Therefore, the foregoing discussions equally apply to solving the initial-boundary value problems and for computing the optimal R_m with time-dependent PDEs. If the temporal domain is large (large T), we employ the block time marching (BTM) scheme (see [10] for details) together with the ELM method for solving the problem. The temporal domain is divided into a number of windows (time blocks) and the problem is computed block by block [10].

When using ELM together with block time marching for time-dependent PDEs, in the pre-processing run for computing the optimal R_m one only needs to use the first time block. In other words, when computing R_{m0} we can use a smaller spatial-temporal domain in the computation, which consists of only the first time block (not the entire temporal domain). The resultant R_{m0} can then be used subsequently in the ELM/BTM simulations for all the time blocks in the entire spatial-temporal domain.

Remark 2.8. When the domain Ω is partitioned into multiple sub-domains and the system (1) is solved by the localELM method (see [10] for details), the procedure for computing the optimal R_m remains essentially the same. The modification lies in that in the system (6) one needs to additionally include the C^k continuity conditions (see [10]) on the collocation points of the sub-domain boundaries. The residual vector in (7) needs to be modified accordingly to include these additional equations.

2.3 ELM Configuration with Multiple R_m Constants (Multi-Rm-ELM)

We next consider a modified ELM method that involves multiple R_m constants for setting the random hidden-layer coefficients, and present a procedure for computing the optimal values of these constants. This modified ELM has the advantage over the conventional ELM from Section 2.2 that it leads to generally more accurate simulation results. The notation below follows that of Section 2.2.

We modify the ELM configuration for solving the system (1) as follows. Instead of setting the coefficients for all the hidden layers to random values from $[-R_m, R_m]$ with a single R_m , we set the weight/bias coefficients for each different hidden layer to random values generated on an interval with a different R_m . Specifically, we set the weight/bias coefficients in hidden layer l , $(\mathbf{W}_l, \mathbf{b}_l)$ for $1 \leq l \leq L-1$, to uniform random values generated on $[-R_m^{(l)}, R_m^{(l)}]$, where $R_m^{(l)}$ ($1 \leq l \leq L-1$) are user-prescribed constants (hyperparameters). The random hidden-layer coefficients are again fixed once they are assigned. This modified ELM provides increased freedom for generating the random hidden-layer coefficients.

Let us consider how to determine the optimal or near-optimal values for these $R_m^{(l)}$ constants. We first generate, for each hidden layer l ($1 \leq l \leq L-1$), a set of $(M_{l-1} + 1)M_l$ uniform random values on the interval $[-1, 1]$, which will be denoted by the vector ξ_l of length $(M_{l-1} + 1)M_l$. Once the random vectors ξ_l ($1 \leq l \leq L-1$) are generated, they will be fixed throughout the computation. Given the constants $R_m^{(l)}$ ($1 \leq l \leq L-1$), the random hidden-layer coefficients $(\mathbf{W}_l, \mathbf{b}_l)$ will be set by the random vector $R_m^{(l)} \xi_l$ for $1 \leq l \leq L-1$. Let $\mathbf{R}_m = (R_m^{(1)}, R_m^{(2)}, \dots, R_m^{(L-1)})$. Then \mathbf{R}_m represents the set of scaling parameters for the random hidden-layer coefficients.

We use a procedure analogous to that of Section 2.2 for computing the optimal \mathbf{R}_m . We solve system (6) by the linear or nonlinear least squares method, and let β_{ij}^{LS} ($1 \leq i \leq M_{L-1}$, $1 \leq j \leq M_L$) denote its least squares solution. Let $\mathbf{u}^{LS}(\mathbf{x}) = \sum_{j=1}^M V_j(\mathbf{x}) \beta_j^{LS}$ denote the least squares solution to the system (1). The residual vector of system (6) at the least squares solution is given by

$$\mathbf{r}(\mathbf{R}_m) = \begin{bmatrix} \vdots \\ \mathbf{L} \left(\sum_{j=1}^M V_j(\mathbf{x}_p, \mathbf{R}_m) \beta_j^{LS} \right) - \mathbf{f}(\mathbf{x}_p) \\ \vdots \\ \vdots \\ \mathbf{B} \left(\sum_{j=1}^M V_j(\mathbf{x}_q, \mathbf{R}_m) \beta_j^{LS} \right) - \mathbf{g}(\mathbf{x}_q) \\ \vdots \end{bmatrix} = \begin{bmatrix} \vdots \\ \mathbf{L}(\mathbf{u}^{LS}(\mathbf{x}_p, \mathbf{R}_m)) - \mathbf{f}(\mathbf{x}_p) \\ \vdots \\ \vdots \\ \mathbf{B}(\mathbf{u}^{LS}(\mathbf{x}_q, \mathbf{R}_m)) - \mathbf{g}(\mathbf{x}_q) \\ \vdots \end{bmatrix} \quad (10)$$

where the dependence on \mathbf{R}_m has been explicitly specified. Note that now \mathbf{r} depends on the multitude of

Algorithm 2: Computing the cost function $\mathcal{N}(\mathbf{R}_m)$ in Multi-Rm-ELM

input : $\mathbf{R}_m = (R_m^{(1)}, \dots, R_m^{(L-1)})$; input data \mathbf{X} ; fixed random vectors $\boldsymbol{\xi}_l$, of length $(M_{l-1} + 1)M_l$ and containing uniform random values on $[-1, 1]$, for $1 \leq l \leq N - 1$.
output: $\mathcal{N}(\mathbf{R}_m)$.

- 1 update the hidden-layer coefficients $(\mathbf{W}_l, \mathbf{b}_l)$ by $R_m^{(l)} \boldsymbol{\xi}_l$, for $1 \leq l \leq L - 1$
 - 2 compute Φ_{L-1} by evaluating the neural network (first $(L - 1)$ layers) on the input data \mathbf{X}
 - 3 solve system (6) for β_{ij}^{LS} by the linear or nonlinear least squares method from [10]
 - 4 update the output-layer coefficients \mathbf{W}_L by β_{ij}^{LS} ($1 \leq i \leq M_{L-1}$, $1 \leq j \leq M_L$)
 - 5 compute \mathbf{u}^{LS} , $\mathbf{L}(\mathbf{u}^{LS})$ and $\mathbf{B}(\mathbf{u}^{LS})$ by evaluating the neural network on \mathbf{X} and by auto-differentiation
 - 6 compute the residual vector $\mathbf{r}(\mathbf{R}_m)$ by equation (10)
 - 7 compute $\mathcal{N}(\mathbf{R}_m)$ by equation (11)
-

$R_m^{(l)}$ ($1 \leq l \leq L - 1$) constants. Consider the Euclidean norm of the residual vector

$$\mathcal{N}(\mathbf{R}_m) = \|\mathbf{r}(\mathbf{R}_m)\|. \quad (11)$$

We seek the optimal value \mathbf{R}_{m0} for \mathbf{R}_m such that $\mathcal{N}(\mathbf{R}_m)$ is minimized, namely,

$$\mathbf{R}_{m0} = \arg \min_{\mathbf{R}_m} \mathcal{N}(\mathbf{R}_m). \quad (12)$$

We solve the optimization problem (12) again by the differential evolution algorithm [47] and employ its scipy implementation. This algorithm requires the valuation routine for the cost function $\mathcal{N}(\mathbf{R}_m)$ for any given \mathbf{R}_m . $\mathcal{N}(\mathbf{R}_m)$ can be evaluated by a modification of the Algorithm 1, and the modified version is summarized in Algorithm 2.

The modified ELM method involves the multiple components of \mathbf{R}_m . An automatic procedure is essential for computing the optimal or near-optimal \mathbf{R}_m in this case. It would be extremely difficult, and practically impossible if the neural network becomes deeper, to determine a near-optimal \mathbf{R}_m manually such as in [10].

Remark 2.9. For neural networks with a single hidden layer, the modified ELM method would contain a single R_m and is therefore identical to the conventional ELM for this case. If the neural network consists of two or more hidden layers, the modified ELM and the conventional ELM will generally be different. It is observed that the modified ELM with multiple R_m constants generally leads to a better accuracy than the conventional ELM, under the same network architecture and the same number of collocation points. The cost for computing the optimal \mathbf{R}_m in the modified ELM is generally larger than that for computing the optimal R_m in the conventional ELM. Note that a list of lower-/upper-bound pairs, each for a component of \mathbf{R}_m , needs to be provided when using the scipy routine of the differential evolution algorithm.

Remark 2.10. Several parameters are important and can influence the accuracy when the differential evolution routine in scipy (`scipy.optimize.differential_evolution`) is invoked. These include the population size, the bounds for R_m (or \mathbf{R}_m), and the relative tolerance for convergence. The size of the population must be at least 4, as required by the differential evolution algorithm [47]. We observe that a population size in the range of 6 to 10 will typically suffice. While a large population size can in principle produce more accurate results, in reality this can make the algorithm harder to converge and take significantly more iterations, with little improvement in the obtained result. As mentioned previously, a pair of bounds $[R_{\min}, R_{\max}]$ for R_m in Single-Rm-ELM (or pairs of bounds for \mathbf{R}_m in Multi-Rm-ELM, each for a component of \mathbf{R}_m) needs to be provided to the routine. Since R_m is in a range of moderate values, we typically employ a range $[0.01, 5]$ (or $[0.01, 3]$) for R_m and also for the \mathbf{R}_m components in the numerical tests. A larger range can ensure that the true optimum R_{m0} will not be missed, but on the other hand may not produce a very accurate R_{m0} under a given maximum number of iterations. An appropriate narrower range is conducive to attaining a more accurate R_{m0} . One can therefore also start out with a larger range to get a rough estimate for R_{m0} , and then narrow down the range based on the rough estimate to obtain a more accurate R_{m0} . The relative tolerance

refers to the tolerance on the ratio between the standard deviation and the mean of the objective function values within the population. A small enough tolerance ensures that all members of the population will reach the minimum upon convergence. We observe that a relative tolerance around 0.1 would typically lead to very good simulation results. Even smaller tolerance values can substantially increase the number of iterations, with little improvement in the obtained results. In the current paper we employ a relative tolerance 0.1 for all the numerical tests in Section 3. In addition to the above parameters, the *scipy* routine can also optionally polish the obtained result in the end using a local minimizer. We observe that the local polishing typically has little or no improvement on the result. In the current paper no polishing is performed on the result from the differential evolution algorithm. We typically employ a maximum of 50 generations in the differential evolution algorithm for the numerical tests.

Remark 2.11. We would like to emphasize that there is one major difference between the current paper and our previous work [10] in terms of the ELM implementation, for computing the $V_j(\mathbf{x})$ (last hidden-layer output fields) and the differential operators involving V_j (see equation (6)). In [10] these differential operators are computed by the default reverse-mode auto-differentiation (“GradientTape”) in Tensorflow. In the current work we have employed the forward-mode auto-differentiation (implemented by the “ForwardAccumulator” in Tensorflow) for computing the differential operators involving $V_j(\mathbf{x})$. This modification has sped up the computations and significantly reduced the ELM network training time in the current paper, when compared with that of [10]. This is because in ELM the number of nodes in the last hidden layer is typically much larger than that of the input layer, which is particularly suitable for forward-mode auto-differentiations.

In the current paper we have compared extensively the current implementation of the ELM method with the finite element method (FEM), including both the classical second-order FEM and the high-order FEM with Lagrange elements [6], in terms of their accuracy and computational cost (FEM computation time, ELM network training time). We observe that, for time-dependent PDEs, the ELM method combined with block time marching consistently and far outperforms the FEM (both 2nd-order and high-order FEM). For stationary PDEs, ELM outperforms FEM (both 2nd-order and high-order FEM) for essentially all problem sizes, except for a range of very small problem sizes. By “outperform” we mean that one method achieves a better accuracy under the same computational budget/cost or incurs a lower computational cost to achieve the same accuracy. These observations can be contrasted with those of [10], where the comparisons between ELM (locELM) and FEM are also performed. In [10] it is observed that: (i) ELM (with the implementation therein) outperforms the classical 2nd-order FEM for larger problem sizes; (ii) ELM is competitive to some degree compared with the high-order FEM, but is not as efficient as the latter. With the improvements in the algorithm and implementation in the current work, the ELM method far outperforms the classical second-order FEM. Furthermore, ELM can markedly outperform the high-order FEM. It is more efficient than or as efficient as the high-order FEM. The comparisons between ELM and the classical and high-order FEMs will be detailed in Section 3.

3 Numerical Examples

In this section we use several numerical examples, with linear/nonlinear and stationary/dynamic PDEs in two dimensions (2D), or in one spatial dimension (1D) plus time for dynamic problems, to demonstrate the effectiveness of the presented method for computing the optimal R_m . We also compare the current improved ELM method with the classical second-order and high-order finite element methods (FEM) with regard to their accuracy and computational cost.

3.1 General Notes on the Implementations

We first provide some implementation notes on the ELM and FEM. They apply to all the numerical tests in the following subsections.

The ELM method is implemented in Python, employing the Tensorflow (www.tensorflow.org) and the Keras (keras.io) libraries. In particular, the differential operators involving the output fields of the last hidden layer are computed using the forward-mode auto-differentiation employing the “ForwardAccumulator” in Tensorflow, as stated before. We use the Gaussian activation function, $\sigma(x) = e^{-x^2}$, in all the hidden nodes for all the test problems in Section 3.

In the pre-processing run for computing the optimum R_{m0} (or \mathbf{R}_{m0}), we have monitored and recorded the wall time for R_{m0} (or \mathbf{R}_{m0}) computation using the “timeit” module in Python. The R_{m0}/\mathbf{R}_{m0} computation time includes all the time spent in the iterations with the differential evolution algorithm and the update of the random hidden-layer coefficients with the final R_{m0} (or \mathbf{R}_{m0}) value upon convergence. Within every differential evolution iteration, the primary computations involve the evaluation of $\mathcal{N}(R_m)$ or $\mathcal{N}(\mathbf{R}_m)$ using the Algorithm 1 or Algorithm 2 for a given R_m or \mathbf{R}_m .

When ELM is used to solve a PDE with a given R_m (or \mathbf{R}_m), the computational cost refers to the training time of the ELM neural network. The ELM network training time includes the computation time for the output fields of the last hidden layer ($V_j(\mathbf{x})$) and the associated differential operators involving these field functions, the computation time for the coefficient matrix and the right hand side for the linear least squares problem, the computation time for the residual of the nonlinear algebraic system and the associated Jacobian matrix for the nonlinear least squares problem, the solution time for the linear/nonlinear least squares problem, and the update time of the output-layer coefficients by the linear/nonlinear least squares solution. Note that, following the protocol in [10], this time does not include, after the network is trained, the evaluation time of the neural network on a set of given data points for the output of the solution data.

In the current paper, the computations for $V_j(\mathbf{x})$ (output fields of the last hidden layer) and the associated differential operators are implemented as “Tensorflow Functions” (tf.function) executed as a computational graph [20]. When these functions are invoked for the first time, the Tensorflow library builds the computational graph by “autograph and tracing” the operations contained in these functions, and performs graph optimizations. When they are invoked subsequently, the computations are performed directly in the graph mode, which generally speeds up the computations significantly. The autograph/tracing operations during the first invocation of the Tensorflow Functions can slow down the computations notably. This means that the network training time when the ELM training routine is invoked for the first time can be markedly larger than that when the training routine is invoked subsequently. We will illustrate this difference with some specific test problems in the following subsections. In the comparisons between ELM and FEM, the ELM network training time refers to the time obtained with the computations in the graph mode (no autograph/tracing).

The finite element method is implemented also in Python, by using the FEniCS library (fenicsproject.org). The FEM implementations for different problems follow those in [10], which we refer the reader to for more detailed discussions.

When FEM is used to solve a given PDE, the computational cost refers to the FEM computation time. The computation time includes the symbolic specifications of the mesh, the finite element space, the trial/test function spaces, the variational problem, the forming and solution of the linear system [10]. All these operations are handled by FEniCS, and are opaque to the user. Note that the FEM computation time does not include the output of the solution data after the problem is solved.

As pointed out in [10], when the FEM code is run for the first time, the FEniCS library compiles the key operations in the Python code into a C++ code using Just-in-Time (JIT) compilers, which is in turn compiled by the C++ compiler and then cached. In subsequent runs of the FEM code, the cached operations are used directly in the FEM computation, making it significantly faster. Therefore, the FEM computation time when the code is run for the first time (with JIT compilation) is considerably larger than that when the code is run subsequently (no JIT compilation). In the comparisons between ELM and FEM for different test problems in the following subsections, the FEM computation time refers to the time collected by “timeit” in subsequent runs of the FEM code (other than the first run, no JIT compilation). All the timing data in this paper are collected on a MAC computer (Intel Core i5 CPU 3.2GHz, 24GB memory) in the authors’ institution.

Here are some further comments on the random number generators. In the current ELM implementation, the random vector $\boldsymbol{\xi}$ in Algorithm 1, the random vectors $\boldsymbol{\xi}_l$ ($1 \leq l \leq L-1$) in Algorithm 2, and the random perturbations in the NLLSQ-perturb method [10] for solving nonlinear PDEs, are all generated by the random number generator from the Tensorflow library. The random numbers involved in the differential evolution routine of the scipy library are generated by the random number generator from the numpy package in Python. In order to make the simulation results reported here exactly reproducible, we employ the same seed value for the random number generators in both Tensorflow and numpy for all the numerical tests in Section 3. In addition, the seed value is fixed for all the numerical experiments within a subsection (see also Remark 2.3). Specifically, the seed value is 1 for the numerical tests in Section 3.2, 10 for those in Section

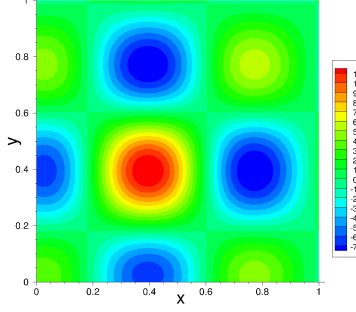


Figure 1: Function approximation: distribution of the function to be approximated.

3.3, 25 for those in Section 3.4, and 100 for those in Section 3.5, respectively. This seed value is passed to the scipy differential evolution routine when invoking that algorithm.

We would like to mention another implementation detail in ELM for all the numerical tests in the following subsections. When implementing the neural network model in Keras, between the input layer (representing (x, y) in 2D or (x, t) in 1D plus time) and the first hidden layer, we have added an affine mapping to normalize the (x, y) or (x, t) data. Suppose $(x, y/t) \in [a_1, b_1] \times [a_2, b_2]$, then this affine mapping normalizes the (x, y) or (x, t) data from $[a_1, b_1] \times [a_2, b_2]$ to the domain $[-1, 1] \times [-1, 1]$. This mapping is implemented as a “lambda” layer in Keras. Because of this affine mapping, all the data into the first hidden layer are normalized. Note that this lambda layer is not counted toward the number of hidden layers in the neural network.

3.2 Function Approximation

In the first example we consider the approximation of a 2D function using ELM and illustrate the effects of the network/simulation parameters on the optimal R_m . The numerical results in this subsection are obtained using a seed value 1 in the random number generators in both Tensorflow and Numpy.

We consider the unit square domain $\Omega = \{(x, y) \mid 0 \leq x, y \leq 1\}$, and the following function on Ω ,

$$f(x, y) = \left[\frac{3}{2} \cos \left(\frac{3}{2} \pi x + \frac{9\pi}{20} \right) + 2 \cos \left(3\pi x - \frac{\pi}{5} \right) \right] \left[\frac{3}{2} \cos \left(\frac{3}{2} \pi y + \frac{9\pi}{20} \right) + 2 \cos \left(3\pi y - \frac{\pi}{5} \right) \right]. \quad (13)$$

Figure 1 illustrates the distribution of this function. Given $f(x, y)$ on a set of data points, we would like to approximate f by ELM. The function approximation problem is equivalent to the problem (1), with $\mathbf{L}(u) = u$ and without the boundary condition (1b). In this case the PDE is reduced to an algebraic equation,

$$u = f(x, y), \quad (14)$$

where $u(x, y)$ is the approximant given in the form of an extreme learning machine.

We use a feedforward neural network to represent $u(x, y)$, with a total of $(L + 1)$ layers. The input layer (layer 0) contains two nodes, representing (x, y) . The output layer (layer L) is linear and contains one node, representing $u(x, y)$. The network consists of one or more hidden layers, with the Gaussian activation function for all the hidden nodes. As stated in Section 2, the network architecture is characterized by the vector $[M_0, M_1, \dots, M_L]$, where M_i denotes the number of nodes in layer i ($0 \leq i \leq L$). The specific architecture of the neural networks are given below. We use $M = M_{L-1}$ to denote the width of the last hidden layer (or number of training parameters). M is either fixed or varied systematically below.

We employ a set of uniform grid points, $Q = Q_1 \times Q_1$, as the collocation points on Ω , where Q_1 denotes the number of uniform collocation points along both x and y directions. Therefore, there are Q_1 uniform collocation points on each boundary of Ω . The input data to the neural network consist of the coordinates of all the collocation points. Q_1 is either fixed or varied systematically in the numerical tests. We assume that the function values $f(x, y)$ are given on the collocation points.

With the above settings, we employ the Single-Rm-ELM and Multi-Rm-ELM configurations from Section 2 to solve this problem. The difference of these two configurations lies in the setting of the random hidden layer coefficients in the neural network, as detailed in Section 2.

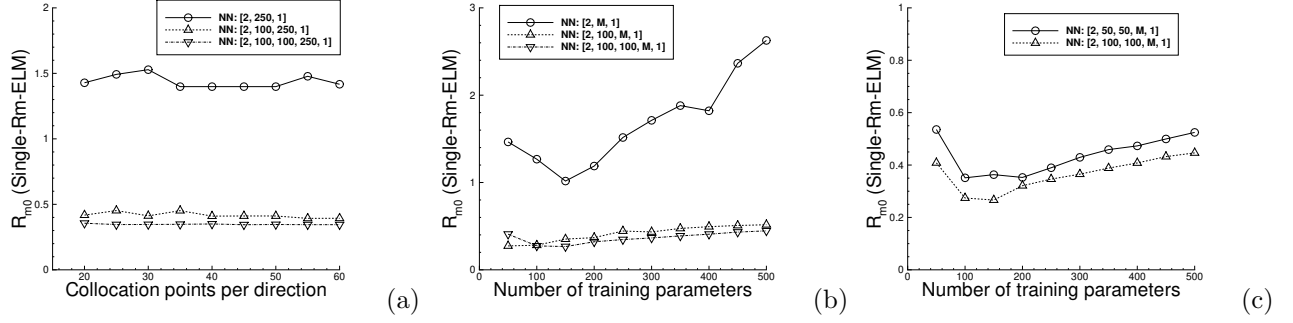


Figure 2: Function approximation (Single-Rm-ELM): The optimum R_{m0} versus (a) the number of collocation points per direction and (b) the number of training parameters, with neural networks of different depth. (c) R_{m0} versus the number of training parameters with neural networks having the same depth but different width. $Q = 31 \times 31$ in (b,c), varied in (a). $M = 250$ in (a), varied in (b,c).

Let us first look into the Single-Rm-ELM configuration, and we employ the method from Section 2.2 to compute the optimal R_m based on the differential evolution algorithm. We have considered several neural network architectures with different depths and widths, and Figure 2 illustrates the characteristics the optimum R_{m0} obtained from the method.

Figure 2(a) depicts the R_{m0} as a function of the number of uniform collocation points in each direction (Q_1) for three neural networks as specified in the legend with one to three hidden layers. The number of training parameters is fixed at $M = 250$, and the widths of the preceding hidden layers are fixed at 100 in them. In this group of tests, for each neural network, we vary the number of collocation points systematically between $Q = 20 \times 20$ and $Q = 60 \times 60$, and for each set of collocation points we compute the optimum R_{m0} . We have employed a population size 6, the bounds $[0.01, 3]$ for R_m , and a relative tolerance 0.1 in the scipy differential evolution routine. We can make two observations from Figure 2(a). First, R_{m0} is largely insensitive to the number of collocation points with Single-Rm-ELM. In other words, R_{m0} remains essentially the same as the number of training data points varies. Second, R_{m0} tends to decrease with increasing number of layers in the neural network. There is a big drop in R_{m0} from a single hidden layer to two hidden layers. Beyond two hidden layers, as the network depth further increases, the decrease in R_{m0} is slight and sometimes almost negligible. These seem to be the common characteristics of R_{m0} with Single-Rm-ELM, which will appear repeatedly in other test problems.

Figure 2(b) shows the effect of the number of training parameters (M) on R_{m0} , with three network architectures as given in the legend. In this group of tests, we employ a fixed set of $Q = 31 \times 31$ uniform collocation points, and vary the number of training parameters systematically between $M = 50$ and $M = 500$. The widths of the preceding hidden layers are fixed at 100 in the tests. Corresponding to each M , we compute the optimum R_{m0} using the differential evolution algorithm. The data in Figure 2(b) correspond to a population size of 8, the R_m bounds $[0.01, 3]$, and a relative tolerance 0.1 in the scipy differential evolution routine. We can make the following observations. First, R_{m0} decreases with increasing depth in the neural network. R_{m0} drops markedly from one hidden layer to two hidden layers in the network. For neural networks with two or more hidden layers, as the depth further increases, R_{m0} decreases only slightly. This observation is consistent with that from Figure 2(a). Second, R_{m0} has a dependence on the number of training parameters. For neural networks with a single hidden layer, this dependence on M is stronger. Figure 2(b) indicates that in this case R_{m0} generally increases with increasing M , except in a range of smaller M values where R_{m0} decreases with increasing M . For neural networks with two or more hidden layers, the dependence of R_{m0} on M is weak. R_{m0} appears to increase only slightly as M increases.

Figure 2(c) illustrates the effect of the widths of the preceding hidden layers on R_{m0} . It depicts the R_{m0} as a function of the number of training parameters (M) for two neural networks, which contain three hidden layers but have different widths (50 versus 100) in the preceding hidden layers (i.e. other than the last hidden layer). These data are obtained again with a population size of 8, the R_m bounds $[0.01, 3]$, and a relative tolerance 0.1 in the differential evolution algorithm. We observe that R_{m0} generally decreases, albeit

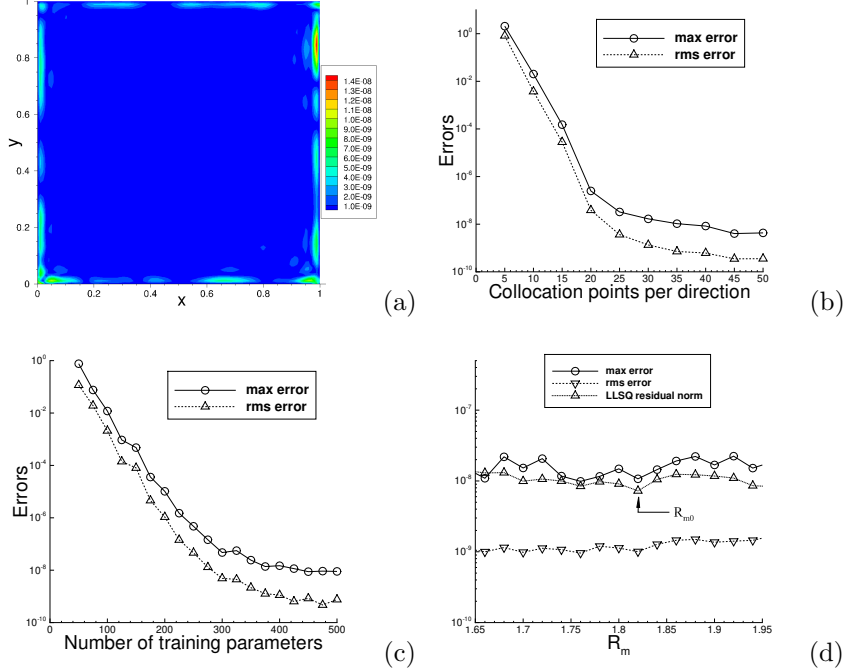


Figure 3: Function approximation (Single-Rm-ELM): (a) absolute-error distribution. The maximum and root-mean-squares (rms) errors in the domain versus (b) the number of collocation points per direction and (c) the number of training parameters (M). (d) The maximum/rms errors and the LLSQ residual norm versus R_m in a neighborhood of R_{m0} . Network architecture: $[2, M, 1]$. $Q = 31 \times 31$ in (a,c,d), varied in (b). $M = 400$ in (a,b,d), varied in (c). $R_m = 1.8$ in (a,b,c), varied in (d). $R_{m0} = 1.822$ in (d).

slightly, as the width of the preceding hidden layers increases. The characteristics observed from Figures 2(b,c) also seem common to Single-Rm-ELM, and they will appear repeatedly in other test problems.

Figure 3 illustrates the accuracy of the ELM approximant with R_m near the optimum R_{m0} in Single-Rm-ELM. In this group of tests, we employ a neural network with an architecture $[2, M, 1]$, where the number of training parameters M is either fixed at $M = 400$ or varied between $M = 50$ and $M = 500$. A set of $Q = Q_1 \times Q_1$ uniform collocation points is employed, where Q_1 is either fixed at $Q_1 = 31$ or varied between $Q_1 = 5$ and $Q_1 = 50$. R_m is either fixed at $R_m = 1.8$, or varied in a neighborhood of $R_{m0} = 1.822$, which is attained from the differential evolution algorithm with $M = 400$ and $Q = 31 \times 31$. Figure 3(a) shows the distribution in the x - y plane of the absolute error of the ELM approximant obtained with $Q = 31 \times 31$, $M = 400$ and $R_m = 1.8$. It indicates that ELM can approximate the function accurately, with the maximum error on the order 10^{-8} . Figure 3(b) shows the maximum and root-mean-squares (rms) errors in the domain of the ELM approximant as a function of Q_1 , which is varied systematically here. It is observed that the errors decrease exponentially with increasing Q_1 before they saturate gradually beyond about $Q_1 \approx 25$. Figure 3(c) shows the maximum/rms errors of the ELM approximant as a function of M , which is varied systematically. We observe an exponential decrease in the errors with increasing M before a gradual saturation for M beyond around $M \approx 300$. Figure 3(d) shows the maximum/rms errors of the ELM approximant, as well as the residual norm of the linear least squares (LLSQ) problem (i.e. $\mathcal{N}(R_m)$ in equation (8)), as a function of R_m in a neighborhood of $R_{m0} = 1.822$. The data indicate that the ELM accuracy is generally not sensitive to R_m within a neighborhood of R_{m0} . The ELM errors are largely comparable with the R_m values around R_{m0} . These results attest to the point in Remark 2.5 that one can generally employ an R_m value around R_{m0} in the computations without seriously sacrificing the accuracy.

Let us next consider the Multi-Rm-ELM configuration for the function approximation problem (14). We employ the method from Section 2.3 to compute the optimum \mathbf{R}_{m0} for neural networks with two or three hidden layers. The results are summarized in Figure 4. In this group of tests, the architecture of the neural

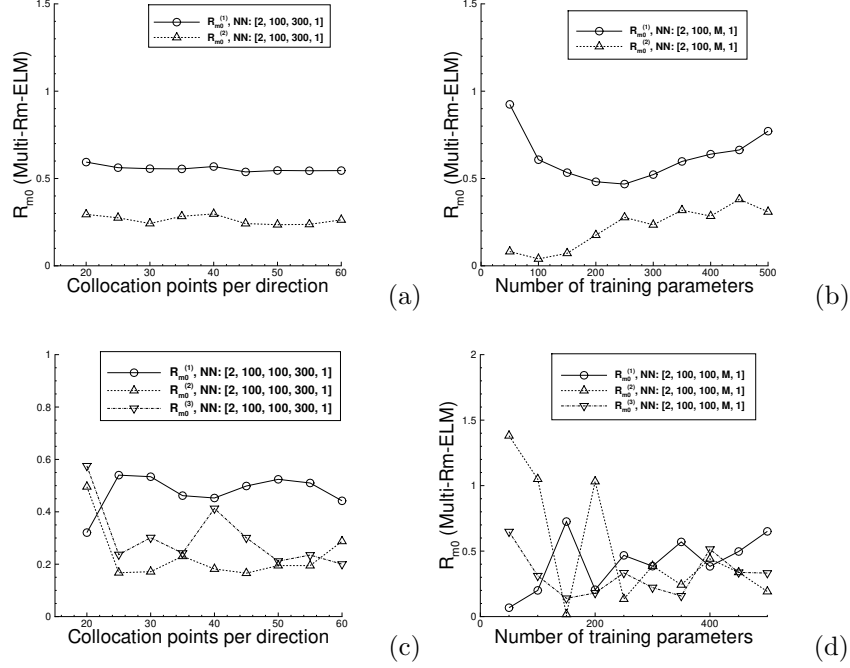


Figure 4: Function approximation (Multi-Rm-ELM): The \mathbf{R}_{m0} components versus the number of collocation points (a,c) and the number of training parameters (b,d), with neural networks having two (a,b) or three (c,d) hidden layers. The network architectures are given in the legends. $Q = 31 \times 31$ in (b,d), varied in (a,c). $M = 300$ in (a,c), varied in (b,d).

networks is characterized by $[2, 100, M, 1]$ or $[2, 100, 100, M, 1]$, where M is either fixed at $M = 300$ or varied between $M = 50$ and $M = 500$. As stated previously, the Gaussian activation function has been employed in all the hidden nodes in this work. We employ a set of $Q = Q_1 \times Q_1$ uniform collocation points in the domain, with Q_1 either fixed at $Q_1 = 31$ or varied between $Q_1 = 20$ and $Q_1 = 60$.

Figures 4(a,b) illustrate the optimum $\mathbf{R}_{m0} = (R_{m0}^{(1)}, R_{m0}^{(2)})$ for the neural networks with two hidden layers, which are obtained with a population size of 10, the bounds $[0.01, 3]$ for all components of \mathbf{R}_m , and a relative tolerance 0.1 in the differential evolution algorithm. Figure 4(a) depicts the \mathbf{R}_{m0} components as a function of Q_1 , with a fixed $M = 300$ in the neural network. We observe that the values for $R_{m0}^{(1)}$ and $R_{m0}^{(2)}$ are quite different, indicating that the random coefficients for the first and second hidden layers could be generated on two quite different intervals. It is also observed that they are essentially independent of the number of collocation points. Figure 4(b) shows the \mathbf{R}_{m0} components as a function of the number of training parameters (M), with a fixed $Q_1 = 31$ in these tests. Both components of \mathbf{R}_{m0} appear to generally increase with increasing M , except that $R_{m0}^{(1)}$ is observed to decrease for a range of smaller M values.

Figures 4(c,d) show the corresponding optimum $\mathbf{R}_{m0} = (R_{m0}^{(1)}, R_{m0}^{(2)}, R_{m0}^{(3)})$ for neural networks containing three hidden layers. These are obtained with a population size of 12, the bounds $[0.01, 3]$ for all components of \mathbf{R}_m , and a relative tolerance 0.1 in the differential evolution algorithm. Figure 4(c) depicts the \mathbf{R}_{m0} components as a function of Q_1 , with a fixed $M = 300$ in the neural network. Figure 4(d) depicts the \mathbf{R}_{m0} components as a function of the number of training parameters M in the neural network, with a fixed set of $Q = 31 \times 31$ uniform collocation points. Overall the relations of the \mathbf{R}_{m0} components with respect to the collocation points and the training parameters appear quite irregular. The relation of \mathbf{R}_{m0} versus the number of collocation points seems somewhat less irregular, and some \mathbf{R}_{m0} components appear to stay close to a constant for a range of Q_1 values. This is in stark contrast to those of Figures 4(a,b) with two hidden layers in the neural network.

Figure 5 illustrates the accuracy of the ELM approximant obtained with Multi-Rm-ELM using an \mathbf{R}_m close to the optimum \mathbf{R}_{m0} . In this group of tests, we employ a neural network with two hidden layers, with its

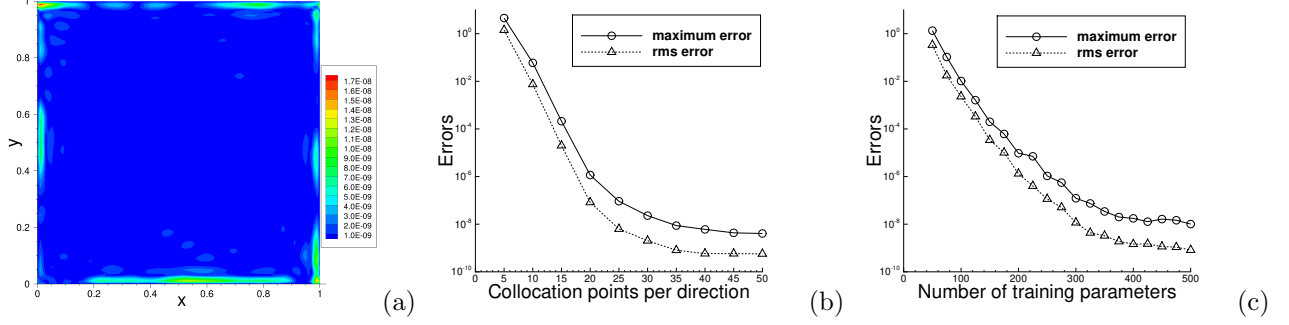


Figure 5: Function approximation (Multi-Rm-ELM): (a) absolute-error distribution of the ELM solution. The maximum/rms errors in the domain versus (b) the number of collocation points per direction, and (c) the number of training parameters M . Network architecture: $[2, 100, M, 1]$. $Q = 31 \times 31$ in (a,c), varied in (b). $M = 400$ in (a,b), varied in (c). $\mathbf{R}_m = (0.6, 0.3)$ in (a,b,c).

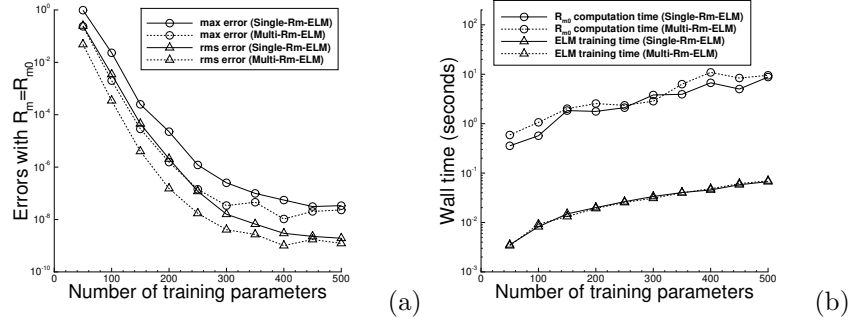


Figure 6: Function approximation: (a) The maximum/rms errors in the domain obtained with $R_m = R_{m0}$ in Single-Rm-ELM and with $\mathbf{R}_m = \mathbf{R}_{m0}$ in Multi-Rm-ELM, versus the number of training parameters (M) in the neural network. (b) The R_{m0} (or \mathbf{R}_{m0}) computation time and the ELM network training time in Single-Rm-ELM and in Multi-Rm-ELM, versus the number of training parameters. Network architecture: $[2, 100, M, 1]$. $Q = 31 \times 31$ in (a,b).

architecture given by $[2, 100, M, 1]$, where M is either fixed at $M = 400$ or varied systematically. We employ a set of $Q = Q_1 \times Q_1$ uniform collocation points, where Q_1 is either fixed at $Q_1 = 31$ or varied systematically. We employ a fixed $\mathbf{R}_m = (0.6, 0.3)$ in Multi-Rm-ELM, which is close to the optimum $\mathbf{R}_{m0} = (0.64, 0.28)$ obtained from the differential evolution algorithm corresponding to $M = 400$ and $Q = 31 \times 31$. Figure 5(a) shows the absolute error distribution of the Multi-Rm-ELM approximant obtained with $M = 400$ and $Q = 31 \times 31$. The approximation is observed to be highly accurate, with a maximum error on the order 10^{-8} in the domain. Figures 5(b) and (c) show the maximum and rms errors of the Multi-Rm-ELM approximants as a function of Q_1 (with a fixed $M = 400$) and as a function of M (with a fixed $Q_1 = 31$), respectively. The results demonstrate the exponential decrease (before saturation) in the errors with respect to the collocation points and the training parameters.

Figure 6 is a comparison of Single-Rm-ELM and Multi-Rm-ELM, with regard to their accuracy and cost for computing the optimal R_m/\mathbf{R}_m with the differential evolution algorithm. In this group of tests we employ a set of $Q = 31 \times 31$ uniform collocation points, and a neural network with an architecture $[2, 100, M, 1]$, where M is varied between 50 and 500.

Figure 6(a) shows the maximum/rms errors of the Single-Rm-ELM (or Multi-Rm-ELM) configuration corresponding to $R_m = R_{m0}$ (resp. $\mathbf{R}_m = \mathbf{R}_{m0}$), as a function of the number of training parameters M in the neural network. The Multi-Rm-ELM errors are observed to be consistently lower, sometimes by over an order of magnitude, than the Single-Rm-ELM errors. This shows that, by setting the hidden-layer coefficients to random values with different maximum magnitudes for different hidden layers, as in the Multi-Rm-ELM

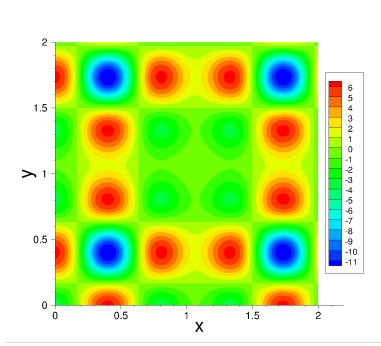


Figure 7: Poisson equation: Distribution of the exact solution.

configuration, one can achieve a better accuracy with the ELM method.

Figure 6(b) shows a comparison of the R_{m0}/\mathbf{R}_{m0} computation time by the differential evolution algorithm, as well as the ELM training time of the neural network, with the Single-Rm-ELM/Multi-Rm-ELM configurations. For both Single-Rm-ELM and Multi-Rm-ELM, R_{m0} and \mathbf{R}_{m0} are computed by using a population size of 10, R_m/\mathbf{R}_m bounds of $[0.01, 3]$, and a relative tolerance 0.1 in the differential evolution algorithm. Note that when computing the R_{m0} (or \mathbf{R}_{m0}) the differential evolution algorithm would invoke the Algorithms 1 or 2 (the ELM training routine) whenever the residual norm for some R_m (or \mathbf{R}_m) needs to be evaluated. The ELM training routine would be typically called dozens of times by the differential evolution algorithm. As shown by Figure 6(b), the R_{m0} (or \mathbf{R}_{m0}) computation time for this function approximation problem is typically on the order of 1 to 10 seconds. In contrast, the ELM network training time for a given R_m is typically on the order of 0.01 to 0.1 seconds for this function approximation problem. From Figure 6(b) we can also observe that computing the \mathbf{R}_{m0} in Multi-Rm-ELM is generally more expensive than computing the R_{m0} in Single-Rm-ELM. Figure 6 indicates that there is a trade-off between the accuracy and the cost for computing the optimal R_m (or \mathbf{R}_m). While the Multi-Rm-ELM is more accurate than the Single-Rm-ELM, the cost for computing the optimal \mathbf{R}_m is also generally larger.

3.3 Poisson Equation

In this subsection we use the canonical 2D Poisson equation to test the method for computing the optimal R_m (or \mathbf{R}_m) and study the effect of the simulation parameters on the optimum R_{m0} (or \mathbf{R}_{m0}). We compare the current ELM method with the classical and high-order FEMs in terms of their computational performance. A seed value 10 is used in the random number generators of Tensorflow and numpy for all the numerical tests in this subsection.

Consider the 2D rectangular domain $\Omega = \{(x, y) \mid 0 \leq x, y \leq 2\}$ and the following boundary value problem with the Poisson equation on Ω and Dirichlet boundary conditions on $\partial\Omega$,

$$\frac{\partial^2 u}{\partial x^2} + \frac{\partial^2 u}{\partial y^2} = f(x, y), \quad (15a)$$

$$u(x, 0) = g_1(x), \quad u(x, 2) = g_2(x), \quad u(0, y) = h_1(y), \quad u(2, y) = h_2(y). \quad (15b)$$

Here $u(x, y)$ is the field to be solved for, $f(x, y)$ is a prescribed source term, and g_1, g_2, h_1 and h_2 are the prescribed boundary distributions. We choose $f(x, y)$ such that the following field satisfies (15a),

$$u(x, y) = - \left[2 \cos \left(\frac{3}{2} \pi x + \frac{2\pi}{5} \right) + \frac{3}{2} \cos \left(3\pi x - \frac{\pi}{5} \right) \right] \left[2 \cos \left(\frac{3}{2} \pi y + \frac{2\pi}{5} \right) + \frac{3}{2} \cos \left(3\pi y - \frac{\pi}{5} \right) \right]. \quad (16)$$

We set g_1, g_2, h_1 and h_2 by evaluating the expression (16) on the corresponding domain boundaries. Under these settings the expression (16) solves the boundary value problem (15). Figure 7 shows the distribution of the analytic solution (16) in the x - y plane.

We solve this problem using ELM. The neural network has an input layer of two nodes (representing x and y), a linear output layer of one node (representing u), and one or more hidden layers in between with

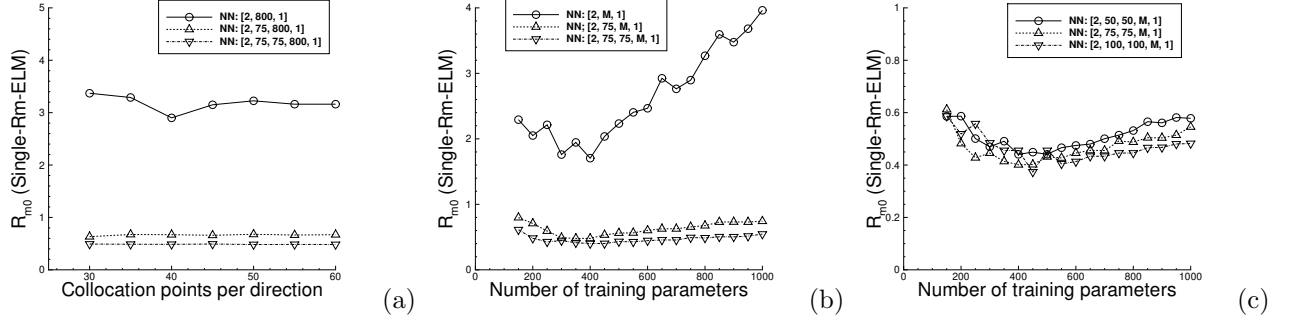


Figure 8: Poisson equation (Single-Rm-ELM): R_{m0} versus (a) the number of collocation points per direction and (b) the number of training parameters, with neural networks of different depth. (c) R_{m0} versus the number of training parameters for neural networks with the same depth but different width. $Q = 35 \times 35$ in (b,c), varied in (a). $M = 800$ in (a), varied in (b,c). Network architectures are listed in the legends.

the Gaussian activation function. The specific architectures of the neural networks will be provided below, again with M denoting the number of training parameters (i.e. the number of nodes of the last hidden layer). We employ a set of $Q = Q_1 \times Q_1$ uniform grid points on Ω as the collocation points, where Q_1 denotes the number of points in both x and y directions. So there are Q_1 uniform collocation points on each domain boundary. Q_1 and M are varied systematically in the numerical tests. We employ the Single-Rm-ELM and Multi-Rm-ELM configurations from Section 2 for setting the random hidden-layer coefficients based on a single R_m or a vector \mathbf{R}_m , respectively.

Figure 8 illustrates the characteristics of the optimum R_{m0} obtained with the differential evolution algorithm for the Poisson equation with the Single-Rm-ELM configuration. Figure 8(a) depicts R_{m0} as a function of Q_1 for several neural networks with different depth. The network architectures are given in the legend, and Q_1 is varied systematically between 30 and 60. Figure 8(b) shows the R_{m0} as a function of the number of training parameters M for several neural networks with different depth. Figure 8(c) shows the computed R_{m0} as a function of M for several neural networks that contain three hidden layers with the same M but different width for the preceding hidden layers. In Figures 8(b,c) a fixed set of $Q = 35 \times 35$ uniform collocation points is employed. In the differential evolution algorithm we have employed a population size of 6, the R_m bounds $[0.1, 5]$ and a relative tolerance of 0.1 for these numerical tests.

We have the following observations from Figure 8. First, R_{m0} is essentially independent of the number of collocation points in the simulation. Second, R_{m0} has a stronger dependence on the number of training parameters M for neural networks containing a single hidden layer, and its dependence on M is quite weak for neural networks with two or more hidden layers. R_{m0} generally increases with increasing M , except in a range with smaller M values where R_{m0} is observed to decrease as M increases. With two or more hidden layers in the neural network, R_{m0} can be approximated by essentially a constant for a wide range of M values. Third, R_{m0} generally decreases with increasing depth of the neural network. It drops significantly from a single hidden layer to two hidden layers, and then decreases only slightly as the depth further increases. Fourth, R_{m0} has only a weak dependence on the width of the preceding hidden layers (other than the last one), and tends to decrease slightly with increasing width of the preceding hidden layers. These observations are consistent with those from the function approximation problem in Section 3.2.

Figure 9 illustrates the solution accuracy obtained with the Single-Rm-ELM configuration. In this group of tests we employ a neural network with an architecture $[2, M, 1]$ and the Gaussian activation function, where the number of training parameters is either fixed at $M = 800$ or varied systematically. The set of uniform collocation points is either fixed at $Q = 35 \times 35$ or varied between $Q = 5 \times 5$ and $Q = 50 \times 50$. We employ a fixed $R_m = 3.36$, which is close to the optimum R_{m0} from the differential evolution algorithm, for generating the random hidden-layer coefficients in Single-Rm-ELM. Figure 9(a) shows the absolute error distribution of the ELM solution in the x - y plane, which corresponds to a fixed $M = 800$ and $Q = 35 \times 35$. It indicates that ELM produces an accurate solution, with the maximum error on the order 10^{-8} . Figures 9(b) and (c) depict the maximum and rms errors in the domain as a function of the number of collocation

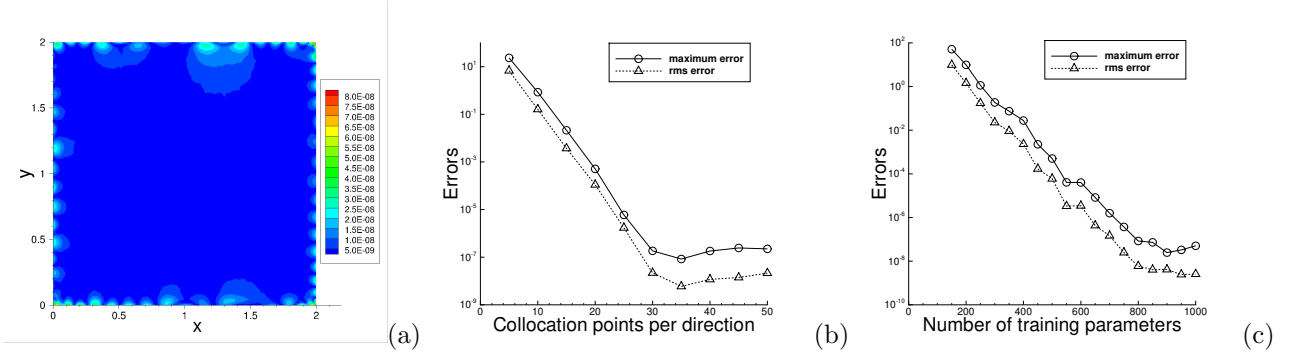


Figure 9: Poisson equation (Single-Rm-ELM): (a) Absolute error distribution of the ELM solution. The maximum/rms errors in the domain versus (b) the number of collocation points per direction and (c) the number of training parameters M . Network architecture: $[2, M, 1]$. $Q = 35 \times 35$ in (a,c), varied in (b). $M = 800$ in (a,b), varied in (c). $R_m = 3.36$ in (a,b,c).

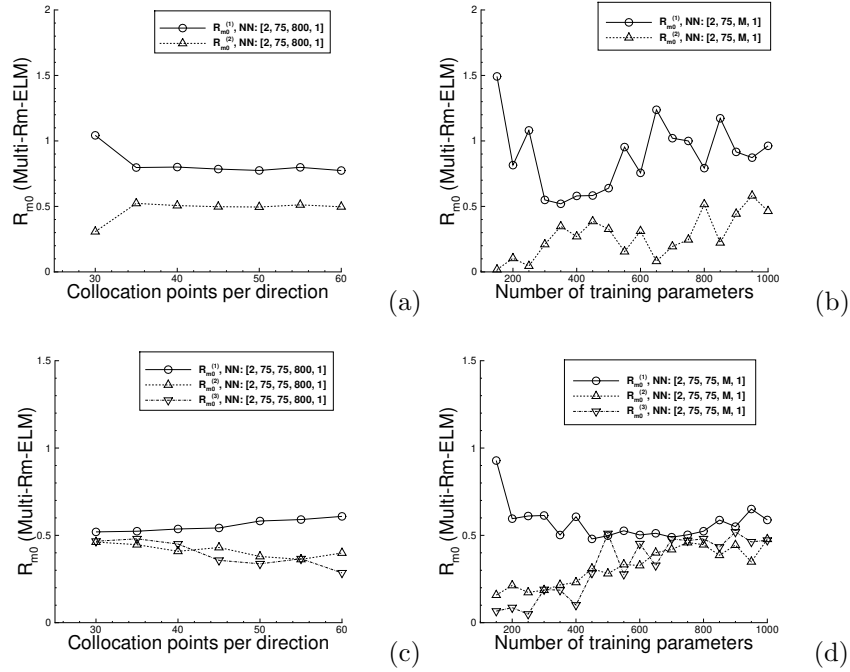


Figure 10: Poisson equation (Multi-Rm-ELM): The optimum \mathbf{R}_{m0} versus the number of collocation points per direction (a,c) and the number of training parameters (b,d), with neural networks having two (a,b) and three (c,d) hidden layers. The network architectures are given in the legends. $Q = 35 \times 35$ in (b,d), varied in (a,c). $M = 800$ in (a,c), varied in (b,d).

points and the number of training parameters, respectively. One can clearly observe that the errors decrease exponentially (before saturation) with increasing number of collocation points and training parameters.

Figure 10 illustrates the characteristics of the optimum \mathbf{R}_{m0} for the Multi-Rm-ELM configuration obtained with the differential evolution algorithm. Here we have considered two neural networks with two and three hidden layers, whose architectures are characterized by $[2, 75, M, 1]$ and $[2, 75, 75, M, 1]$, respectively, where M is either fixed at $M = 800$ or varied systematically. A set of uniform collocation points is employed, either fixed at $Q = 35 \times 35$ or varied systematically between $Q = 30 \times 30$ and $Q = 60 \times 60$. Figures 10(a) and (b) show the components of $\mathbf{R}_{m0} = (R_{m0}^{(1)}, R_{m0}^{(2)})$ versus the number of collocation points and the number of training parameters for the neural network with two hidden layers, respectively. These are obtained with

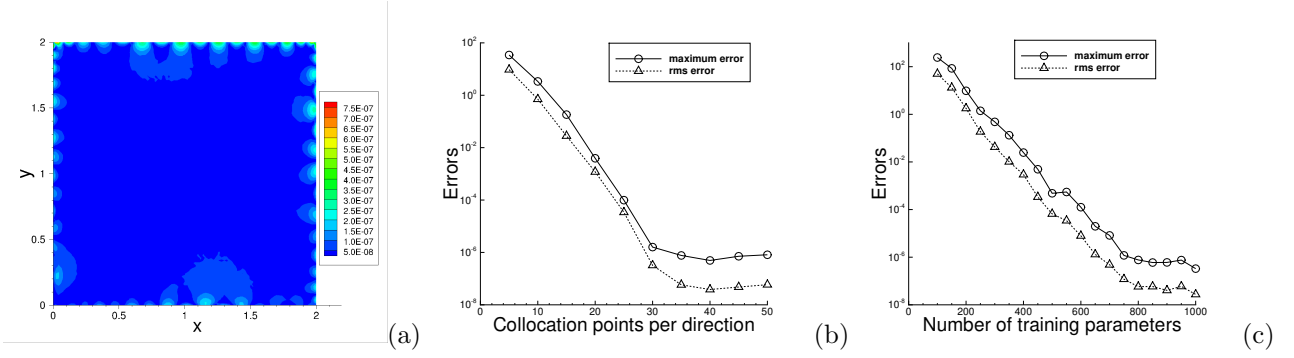


Figure 11: Poisson equation (Multi-Rm-ELM): (a) Absolute error distribution of the Multi-Rm-ELM solution. The maximum/rms errors in the domain versus (b) the number of collocation points per direction, and (c) the number of training parameters. Network architecture: $[2, 75, M, 1]$. $Q = 35 \times 35$ in (a,c), varied in (b). $M = 800$ in (a,b), varied in (c). $\mathbf{R}_m = (0.8, 0.5)$ in (a,b,c).

a population size of 8, the bounds $[0.01, 3]$ for all \mathbf{R}_m components, and a relative tolerance of 0.1 in the differential evolution algorithm. Figures 10(c) and (d) show the components of $\mathbf{R}_{m0} = (R_{m0}^{(1)}, R_{m0}^{(2)}, R_{m0}^{(3)})$ versus the number of collocation points and the number of training parameters for the neural network with three hidden layers, respectively. They are obtained using a population size of 9, the bounds $[0.01, 3]$ for all the \mathbf{R}_m components, and a relative tolerance of 0.1 in the differential evolution algorithm. One can see that the \mathbf{R}_{m0} components exhibit a fairly weak dependence (Figure 10(c)) or essentially no dependence (Figure 10(a)) on the number of the collocation points in the domain. The relation between \mathbf{R}_{m0} and the number of training parameters, on the other hand, appears quite irregular. The \mathbf{R}_{m0} components tend to increase as the number of training parameters M increases, except for some component, which appears to decrease in a range of smaller M values.

Figure 11 illustrates the solution accuracy obtained with the Multi-Rm-ELM configuration. In this group of tests we employ a neural network with two hidden layers, with an architecture $[2, 75, M, 1]$, where M is either fixed at $M = 800$ or varied systematically. The set of uniform collocation points is either fixed at $Q = 35 \times 35$ or varied between $Q = 5 \times 5$ and $Q = 50 \times 50$. We employ a fixed $\mathbf{R}_m = (0.8, 0.5)$ here, close to the \mathbf{R}_{m0} obtained corresponding to $M = 800$ and $Q = 35 \times 35$. Figure 11(a) shows the distribution of the absolute error of the Multi-Rm-ELM solution corresponding to $M = 800$ and $Q = 35 \times 35$, suggesting a quite high accuracy, with the maximum error on the order 10^{-7} . Figures 11(b) and (c) depict the maximum/rms errors in the domain as a function of the number of collocation points and the training parameters, respectively. The exponential convergence of the errors (before saturation) with respect to the collocation points and the training parameters is evident.

Figure 12 is a comparison between the Single-Rm-ELM and the Multi-Rm-ELM methods in terms of their accuracy and R_{m0}/\mathbf{R}_{m0} computation cost. Here we consider two neural networks with architectures $[2, 75, M, 1]$ and $[2, 75, 75, M, 1]$, respectively, where M is varied systematically. We employ a set of $Q = 35 \times 35$ uniform collocation points in the domain. We look into the numerical errors corresponding to $R_m = R_{m0}$ in Single-Rm-ELM and $\mathbf{R}_m = \mathbf{R}_{m0}$ in Multi-Rm-ELM, and the time spent on computing R_{m0} and \mathbf{R}_{m0} with the differential evolution algorithm, as well as the networking training time with ELM for solving the Poisson equation with the obtained R_{m0} or \mathbf{R}_{m0} . Figures 12(a) and (c) depict the maximum/rms errors in the domain as a function of the number of training parameters M for these two neural networks, respectively, obtained with $R_m = R_{m0}$ in Single-Rm-ELM and $\mathbf{R}_m = \mathbf{R}_{m0}$ in Multi-Rm-ELM. Figures 12(b) and (d) depict the corresponding R_{m0} and \mathbf{R}_{m0} computation time with the differential evolution algorithm, as well as the ELM network training time, versus M . The R_{m0} and \mathbf{R}_{m0} computations in Figures 12(a) and (b), for the neural network with two hidden layers, correspond to a population size of 10, the R_m and \mathbf{R}_m bounds $[0.01, 3]$, and a relative tolerance 0.1 in the differential evolution algorithm with both Single-Rm-ELM and Multi-Rm-ELM. The R_{m0} and \mathbf{R}_{m0} computations in Figures 12(c) and (d), for three hidden layers in the neural network, correspond to a population size of 9 and the same bounds and relative tolerance as in (a,b) for both Single-Rm-ELM and Multi-Rm-ELM.

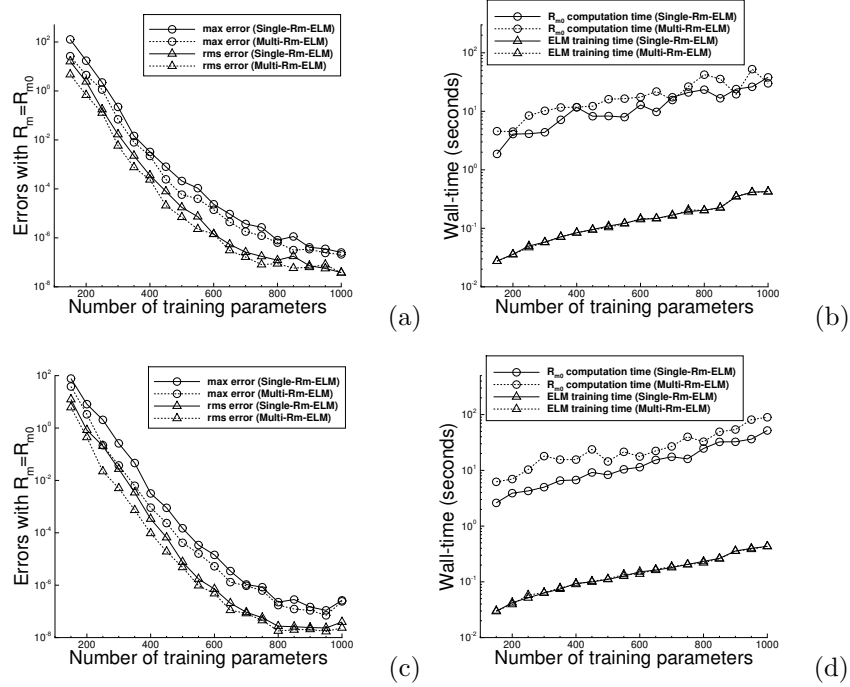


Figure 12: Poisson equation: (a,c) The maximum/rms errors in the domain corresponding to $R_m = R_{m0}$ in Single-Rm-ELM and $\mathbf{R}_m = \mathbf{R}_{m0}$ in Multi-Rm-ELM, versus the number of the training parameters (M). (b,d) The R_{m0} (or \mathbf{R}_{m0}) computation time and the ELM network training time in Single-Rm-ELM and Multi-Rm-ELM, versus the number of training parameters (M). Network architecture: $[2, 75, M, 1]$ in (a,b), $[2, 75, 75, M, 1]$ in (c,d). $Q = 35 \times 35$ in (a,b,c,d).

We can make the following observations from Figure 12. First, the Multi-Rm-ELM method consistently leads to smaller numerical errors than Single-Rm-ELM. By setting the weight/bias coefficients in different hidden layers to random values with different maximum magnitudes as given by \mathbf{R}_m , Multi-Rm-ELM can produce more accurate results than Single-Rm-ELM, which sets the weight/bias coefficients in all hidden layers to random values with the same maximum magnitude R_m . Second, the cost for computing \mathbf{R}_{m0} in Multi-Rm-ELM is generally higher than that for computing R_{m0} in Single-Rm-ELM. Third, for a given R_m in Single-Rm-ELM and given \mathbf{R}_m in Multi-Rm-ELM, the ELM network training time for solving the Poisson equation is essentially the same. Fourth, the R_{m0}/\mathbf{R}_{m0} computation cost with differential evolution is markedly higher than the ELM network training cost for solving the PDE with a given R_m or \mathbf{R}_m .

As discussed in Section 3.1, the computations for the output fields of the last hidden layer and the associated differential operators are implemented as “Tensorflow Functions” in this paper, which are executed as a computational graph. When these functions are invoked for the first time, autograph/tracing occurs in Tensorflow to build the computational graph, which can slow down the computations. Subsequent invocations of these functions are executed in the graph mode, which is much faster. Figure 13 illustrates this effect for solving the Poisson equation. Figure 13(a) depicts the ELM network training time with the Single-Rm-ELM configuration, with the training routine invoked for the first time and invoked subsequently, as a function of the number of collocation points in each direction. Figure 13(b) depicts the corresponding ELM network training time as a function of the number of training parameters in the neural network. The settings and the simulation parameters here correspond to those of Figures 9(b) and (c), respectively. One can observe that the ELM training time is reduced dramatically when these computations are performed in the graph mode (without autograph/tracing).

We next compare the computational performance, accuracy and computational cost, between the current implementation of ELM and the finite element method (classical second-order FEM, and high-order FEM) for solving the Poisson equation. For ELM we use the Single-Rm-ELM configuration in the following com-

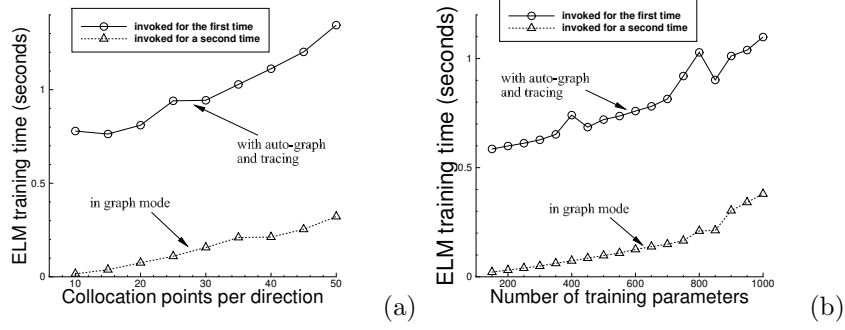


Figure 13: Poisson equation (Single-Rm-ELM): ELM network training time versus (a) the number of collocation points per direction and (b) the number of training parameters, obtained with the training routine invoked for the first time or subsequently. In the first invocation auto-graph/tracing occurs to build the computational graphs, which are used in the graph mode in subsequent invocations. The settings and parameters here correspond to those of Figures 9(b,c).

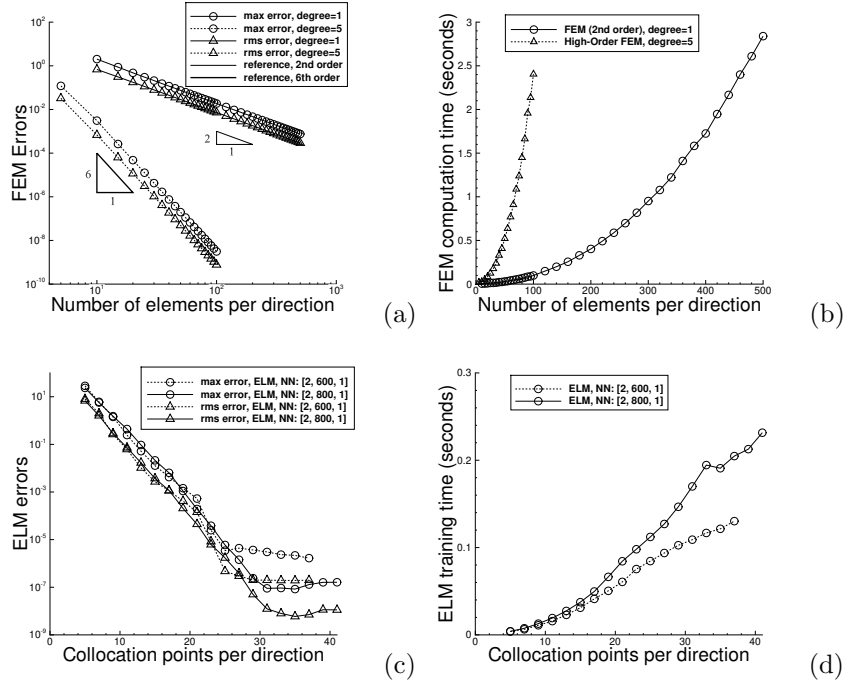


Figure 14: Poisson equation: The numerical errors (a) and the computation time (b) of the classical FEM (2nd-order, linear elements or degree=1) and the high-order FEM (Lagrange elements, degree 5), versus the number of elements in each direction. The numerical errors (c) and the network training time (d) of ELM (Single-Rm-ELM) versus the number of collocation points per direction. ELM network architectures are given in the legends of (c,d). $R_m = 2.76$ for $M = 600$ and $R_m = 3.36$ for $M = 800$ in (c,d). The ELM network training time is the time obtained in the graph mode (no autograph/tracing).

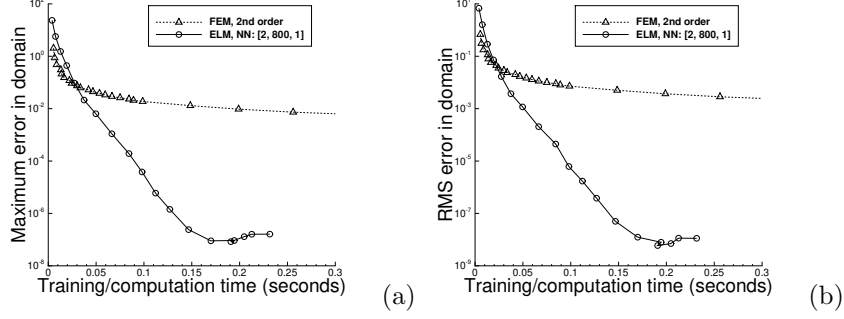


Figure 15: Poisson equation (comparison between ELM and classical FEM): The (a) maximum error and (b) rms error in the domain versus the computational cost (ELM training time, FEM computation time) for ELM and the classical FEM. The FEM data correspond to those of Figures 14(a,b) with degree=1. The ELM data correspond to those of Figures 14(c,d) with $M = 800$.

parisons. For FEM, as stated in Section 3.1, it is implemented using the FEniCS library as in [10]. The classical FEM employs Lagrange elements of degree one (linear elements), and high-order FEM employs Lagrange elements [6] with degrees larger than one from the FEniCS library. When solving the boundary value problem (15) using FEM, we partition the domain Ω into an $N_1 \times N_1$ rectangular mesh, where N_1 is the number of rectangles in each direction. Each rectangle is further partitioned into two triangular elements along the diagonal. So a total of $2N_1^2$ triangular elements are involved in the FEM computation. For convenience we will loosely refer to N_1 as the number of elements in each direction. In the FEM tests we vary the number of elements per direction N_1 and the degree of the Lagrange elements systematically.

Another implementation detail with FEM concerns the evaluation of the source term and the Dirichlet boundary data in equations (15a)–(15b). These terms each is implemented as a FEniCS “Expression”, in which the degree parameter is specified as the element degree plus one when solving the Poisson equation. We observe that if the degree parameter in these FEniCS Expressions is specified to be equal to the element degree or less, one cannot seem to quite achieve the expected convergence rate as the number of elements increases, especially when the mesh size is not very large.

Figure 14 provides an overview of the numerical errors of FEM and ELM, as well as their computational cost (FEM computation time, ELM network training time). In these tests the number of the elements in the FEM mesh and the number of collocation points in ELM are varied systematically.

Figure 14(a) shows the maximum/rms errors in the domain as a function of the number of elements in each direction (N_1) with the classical FEM (degree=1) and the high-order FEM with Lagrange elements of degree=5. One can clearly observe a second-order convergence rate and a sixth-order convergence rate with these two types of elements. Figure 14(b) shows the corresponding FEM computation time versus the number of elements per direction with these two types of elements. The FEM computation time grows quite rapidly with increasing number of elements. The cost of the high-order FEM grows much faster than that of the classical FEM.

Figure 14(c) shows the ELM maximum/rms errors in the domain as a function of the number of uniform collocation points in each direction, obtained using two neural networks with the architectures $[2, M, 1]$ with $M = 600$ and $M = 800$, respectively. We have employed $R_m = 2.76$ for $M = 600$ and $R_m = 3.36$ for $M = 800$, close to their optimal R_{m0} , for generating the random hidden layer coefficients. A set of $Q = Q_1 \times Q_1$ uniform collocation points is employed and Q_1 is varied systematically. One can clearly observe an exponential decrease in the ELM errors before saturation. As Q_1 becomes sufficiently large, the ELM errors saturate at a higher level with $M = 600$ than with $M = 800$. Figure 14(d) shows the corresponding ELM network training time versus the number of collocation points per direction with these two neural networks. Here the ELM training time refers to the time obtained with the graph mode (no autograph/tracing). They appear to grow quasi-linearly with increasing number of collocation points.

Figure 15 compares the computational performance of the ELM and the classical FEM. The two plots show the maximum and rms errors in the domain of the ELM and FEM versus their computational cost

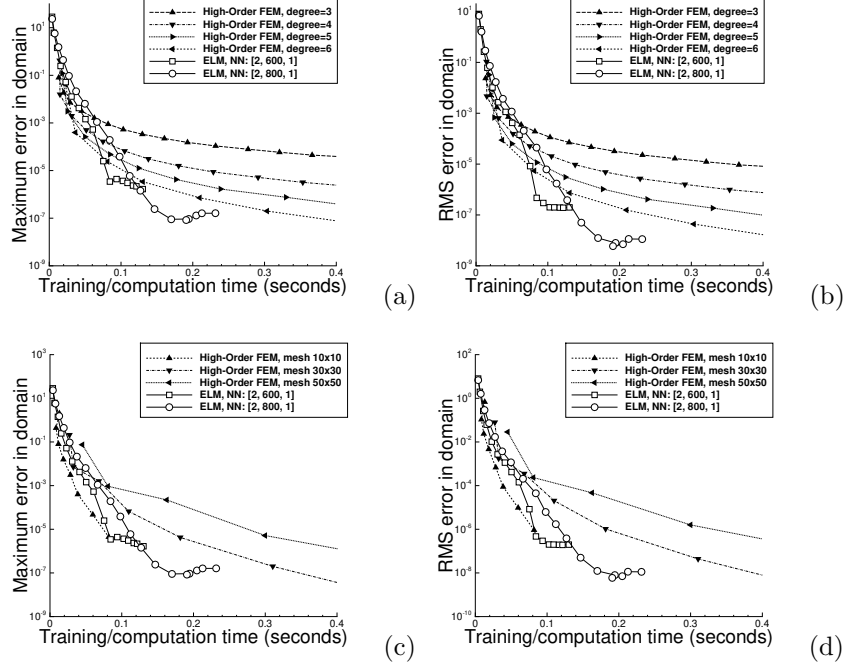


Figure 16: Poisson equation (comparison between ELM and high-order FEM): The maximum error (a,c) and the rms error (b,d) in the domain versus the computational cost (ELM network training time, FEM computation time) of the ELM and the high-order FEM with Lagrange elements of various degrees. For FEM, in (a,b) the mesh size is varied systematically for each given element degree, and in (c,d) the element degree is varied systematically for each given mesh size. The FEM data in (a,b) with degree=5 correspond to those of Figures 14(a,b) with degree=5. The ELM data in (a,b,c,d) correspond to those of Figures 14(c,d).

(FEM computation time, ELM network training time). The FEM data here correspond to those contained in Figures 14(a,b) with degree=1, and the ELM data here correspond to those of Figures 14(c,d) with $M = 800$. We observe that the ELM far outperforms the classical FEM in essentially all cases, except for a narrow range with very small problem sizes (FEM mesh size below around 50×50 , ELM collocation points below around 13×13 ; error level above around 5×10^{-2} ; wall time below around 0.03 seconds). With the same computational cost/budget, the ELM achieves a considerably better accuracy (typically by orders of magnitude) than the classical FEM, and to achieve the same accuracy the ELM incurs a much lower computational cost than the classical FEM. Even in the narrow range of small problem sizes, where the classical FEM is a little better, the FEM performance and the ELM performance are quite close.

Figure 16 provides a comparison of the computational performance between the ELM and the high-order FEM with Lagrange elements of higher degrees. We have conducted two groups of tests with high-order FEM. In the first group, for a fixed element degree, we vary the mesh size systematically. In the second group, for a fixed mesh size, we vary the degree of the Lagrange elements systematically (between 2 and 8). These two types of tests approximately correspond to the so-called h-type and p-type refinements with the high-order hp-finite element method [30, 48, 9].

Figures 16(a) and (b) show the maximum and rms errors in the domain of the high-order FEM, with Lagrange elements of degrees ranging from 3 to 6, versus the FEM computation time in the first group of tests. The FEM data with degree=5 in these plots correspond to those of Figures 14(a,b) with degree=5. Figures 16(c) and (d) depict the maximum/rms errors of the high-order FEM, with mesh sizes ranging from 10×10 to 50×50 , versus the FEM computation time in the second group of tests. In all these plots, we have included the ELM maximum/rms errors versus the ELM network training time for comparison, where the ELM data correspond to those contained in Figures 14(c,d) with $M = 600$ and $M = 800$.

We can make the following observations from Figure 16. With the h-type refinement (for a fixed element

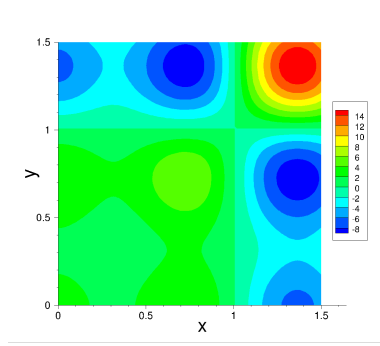


Figure 17: Nonlinear Helmholtz equation: distribution of the exact solution.

degree), there is a cross-over point with respect to the problem size in the relative performance between ELM and high-order FEM. For smaller problem sizes (smaller FEM mesh, smaller set of ELM collocation points), the performance of the ELM and that of the high-order FEM are largely comparable, with the high-order FEM being a little better. For larger problem sizes, the ELM outperforms the high-order FEM markedly (see Figures 16(a,b)). With the p-type refinement (for a fixed mesh size), there is also a cross over in the relative performance between ELM and high-order FEM with respect to the mesh size. With a small FEM mesh size, the performance of the high-order FEM (with varying element degree) and that of the ELM are comparable, with the high-order FEM being a little better. With a larger FEM mesh size, the ELM markedly outperforms the high-order FEM with varying element degree, especially for larger FEM degrees (see Figures 16(c,d)). Overall, we observe that the ELM method is very competitive compared with the high-order FEM. For small problem sizes, the ELM performance and the high-order FEM performance appear largely comparable, with the high-order FEM oftentimes a little better. For larger problem sizes, the ELM method outperforms the high-order FEM. As the problem size becomes large, ELM can outperform the high-order FEM by a substantial factor.

These observations on the ELM/FEM performance should be compared with those of [10]. In [10], it is observed that the ELM method can outperform the classical 2nd-order FEM for larger problem sizes. Compared with high-order FEM, however, ELM (with the implementation therein) is observed to be generally not as competitive [10]. With the improvements in the current work, especially the use of forward-mode auto-differentiations for computing the differential operators (see Remark 2.11), we have significantly increased the ELM computational performance. As shown above, the improved ELM herein far outperforms the classical FEM. Its computational performance is on par with that of the high-order FEM, and oftentimes it can outperform the high-order FEM by a substantial margin.

3.4 Nonlinear Helmholtz Equation

We next use a nonlinear Helmholtz type equation in 2D to further test the method for computing the optimal R_m and \mathbf{R}_m . We demonstrate the competitiveness of the ELM method for nonlinear problems by comparing its performance with those of the classical and high-order FEMs. A seed value 25 has been employed with the random number generators in Tensorflow and numpy for all the numerical tests in this subsection.

Consider a 2D rectangular domain $\Omega = \{(x, y) \mid 0 \leq x, y \leq 1.5\}$ and the following boundary value problem on Ω ,

$$\frac{\partial^2 u}{\partial x^2} + \frac{\partial^2 u}{\partial y^2} - 100u + 10 \cos(2u) = f(x, y), \quad (17a)$$

$$u(x, 0) = g_1(x), \quad u(x, 1.5) = g_2(x), \quad u(0, y) = h_1(y), \quad u(1.5, y) = h_2(y). \quad (17b)$$

In the above equations, $u(x, y)$ is the field to be solved for, f is a prescribed source term, and g_1 , g_2 , h_1 and h_2 are prescribed Dirichlet boundary data. We choose the source term and the boundary data appropriately

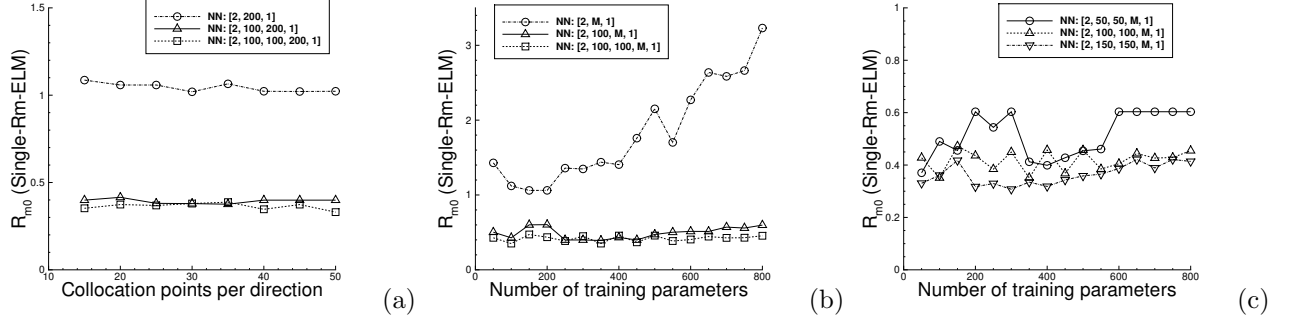


Figure 18: Nonlinear Helmholtz equation (Single-Rm-ELM): The optimum R_{m0} versus (a) the number of collocation points per direction and (b) the number of training parameters, with neural networks of different depth. (c) R_{m0} versus the number of training parameters with neural networks having the same depth but different width. $Q = 31 \times 31$ in (b,c), varied in (a). $M = 200$ in (a), varied in (b,c). The network architectures are given in the legends.

so that the following field satisfies the problem (17),

$$u(x, y) = \left[\frac{5}{2} \cos \left(\pi x - \frac{2\pi}{5} \right) + \frac{3}{2} \cos \left(2\pi x + \frac{3\pi}{10} \right) \right] \left[\frac{5}{2} \cos \left(\pi y - \frac{2\pi}{5} \right) + \frac{3}{2} \cos \left(2\pi y + \frac{3\pi}{10} \right) \right]. \quad (18)$$

The distribution of the analytic solution (18) in the x - y plane is shown in Figure 17.

The settings of the ELM neural network are similar to those in Section 3.3. The input layer contains two nodes, representing x and y . The output layer is linear and contains one node, representing u . The network contains one or more hidden layers, with the Gaussian activation function for all hidden nodes. The random hidden-layer coefficients are set based on the Single-Rm-ELM or Multi-Rm-ELM configurations as described in Section 2. The neural network is trained by the NLLSQ-perturb method from [10], as discussed in Section 2. The crucial simulation parameters include the number of training parameters M , the set of $Q = Q_1 \times Q_1$ uniform collocation points in the domain, and the maximum magnitude R_m or \mathbf{R}_m of the random coefficients.

We first look into the Single-Rm-ELM configuration for assigning the random coefficients in the neural network. Figure 18 illustrates the characteristics of the optimum R_{m0} in Single-Rm-ELM obtained by the differential evolution algorithm. Note that when computing R_{m0} with differential evolution, we have turned off the random perturbations and the corresponding sub-iterations in the NLLSQ-perturb method, as discussed in Remark 2.6. In these tests we consider one to three hidden layers in the neural network, and vary the number of collocation points per direction Q_1 or the number of training parameters M systematically.

Figure 18(a) depicts the optimum R_{m0} as a function of Q_1 , for three neural networks with a fixed number of 200 training parameters but different depth. Figures 18(b) and (c) each depicts the R_{m0} as a function of M for three neural networks. The three neural networks in plot (b) have different depths, with one to three hidden layers and with the width fixed at 100 for the hidden layers other than the last one. The three neural networks in plot (c) all contain three hidden layers, but the width the preceding hidden layers (other than the last one) varies between 50 and 150. In both (b) and (c), the number of nodes in the last hidden layer (i.e. M) is varied systematically, and a fixed set of $Q = 31 \times 31$ uniform collocation points is employed. All these results about R_{m0} are obtained with a population size of 4 and a relative tolerance 0.1 in the differential evolution algorithm. The R_m bounds are $[0.1, 3]$ in the differential evolution algorithm for all the cases except for the neural network with the architecture $[2, M, 1]$ in Figure 18(b), in which the R_m bounds are set to $[0.1, 4]$.

We observe from Figure 18 the same characteristics about R_{m0} for the nonlinear Helmholtz equation as those for the linear problems in previous subsections. For example, R_{m0} is largely independent of the number of collocation points. It generally decreases with increasing number of layers in the neural network. There is a large decrease in R_{m0} from one to two hidden layers in the network, and beyond that the decrease in R_{m0} is almost negligible.

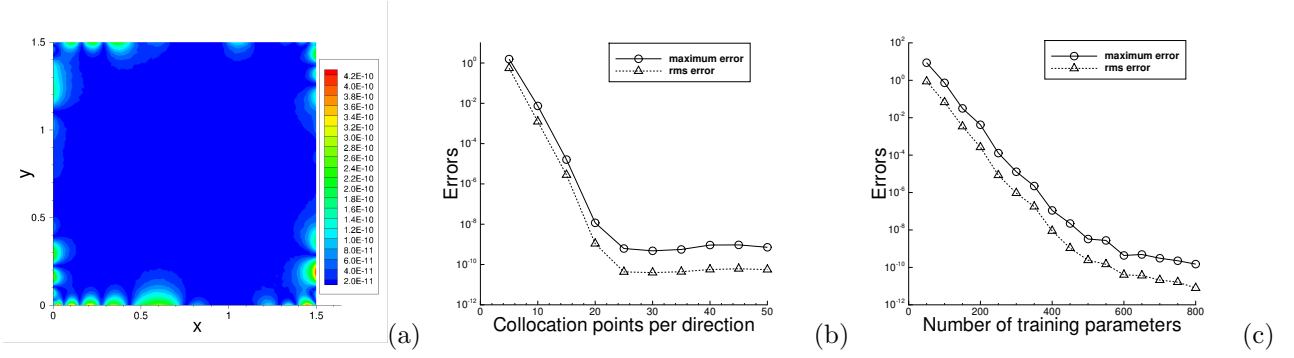


Figure 19: Nonlinear Helmholtz equation (Single-Rm-ELM): (a) Absolute error distribution of the Single-Rm-ELM solution. The maximum/rms errors in the domain versus (b) the number of collocation points per direction, and (c) the number of training parameters. Network architecture: $[2, M, 1]$. $Q = 31 \times 31$ in (a,c), varied in (b). $M = 600$ in (a,b), varied in (c). $R_m = 2.1$ in (a,b,c).

Figure 19 illustrates the accuracy of the solutions to the nonlinear Helmholtz equation obtained with Single-Rm-ELM. In these tests we employ a set of $Q = Q_1 \times Q_1$ uniform collocation points, where Q_1 is either fixed at $Q_1 = 31$ or varied systematically, a neural network with the architecture $[2, M, 1]$, where M is either fixed at $M = 600$ or varied systematically. We employ a fixed $R_m = 2.1$ in these tests, which is close to the R_{m0} from the differential evolution algorithm corresponding to $M = 600$ and $Q = 31 \times 31$. Figure 19(a) shows the distribution of the absolute error of the Single-Rm-ELM solution. It signifies a high solution accuracy, with the maximum error on the order 10^{-10} . Figures 19(b) and (c) depict the maximum/rms errors in the domain of the ELM solution as a function of Q_1 and the training parameters M , respectively. The errors decrease exponentially (before saturation) with increasing numbers of collocation points or training parameters, similar to what has been observed for the linear problems in previous subsections.

Let us next consider the Multi-Rm-ELM configuration for setting the random coefficients in the neural network. Figure 20 illustrates the characteristics of the optimum \mathbf{R}_{m0} obtained with the differential evolution algorithm, as the number of collocation points or training parameters is varied. In these tests we consider two neural networks with architectures given by $[2, 100, M, 1]$ and $[2, 100, 100, M, 1]$, respectively, where the number of training parameters is either fixed at $M = 300$ or varied systematically. A set of $Q = Q_1 \times Q_1$ uniform collocation points is employed, where Q_1 is either fixed at $Q_1 = 31$ or varied systematically. Figures 20(a) and (b) depict the components of $\mathbf{R}_{m0} = (R_{m0}^{(1)}, R_{m0}^{(2)})$ as a function of Q_1 and M , respectively, for the neural network with two hidden layers. These results are obtained with a population size of 4, the bounds $[0.01, 3]$ for both \mathbf{R}_m components, and a relative tolerance 0.1 in the differential evolution algorithm. Figures 20(c) and (d) show the corresponding results for $\mathbf{R}_{m0} = (R_{m0}^{(1)}, R_{m0}^{(2)}, R_{m0}^{(3)})$ with the neural network of three hidden layers, which are obtained with a population size of 6, the bounds $[0.01, 2]$ for all \mathbf{R}_m components, and a relative tolerance 0.1 in the differential evolution. The \mathbf{R}_{m0} characteristics observed here are quite similar to those of the linear problems in previous subsections. The values for the \mathbf{R}_{m0} components fluctuate within a range (generally less than 1), and appear more irregular compared with the R_{m0} in Single-Rm-ELM. The dependence of \mathbf{R}_{m0} on the collocation points seems generally quite weak. Its relation to the number of training parameters is quite irregular, especially with more hidden layers in the neural network.

Figure 21 illustrates the accuracy of the Multi-Rm-ELM solutions. In these tests we employ a neural network with an architecture $[2, 100, M, 1]$, where the number of training parameters is either fixed at $M = 500$ or varied systematically. A set of $Q = Q_1 \times Q_1$ uniform collocation points is used, with Q_1 fixed at $Q_1 = 31$ or varied systematically. We employ a fixed $\mathbf{R}_m = (0.54, 0.4)$ in Multi-Rm-ELM, which is close to the \mathbf{R}_{m0} obtained with $M = 500$ and $Q = 31 \times 31$. Figure 21(a) shows the distribution of the absolute error of the Multi-Rm-ELM solution corresponding to $Q_1 = 31$ and $M = 500$, signifying a quite high accuracy with the maximum error on the order 10^{-9} . Figures 21(b) and (c) depict the maximum and rms errors in the domain of the Multi-Rm-ELM solution versus Q_1 and M , respectively, demonstrating the exponential convergence (before saturation) with respect to these parameters.

A comparison between Single-Rm-ELM and Multi-Rm-ELM for the nonlinear Helmholtz equation is

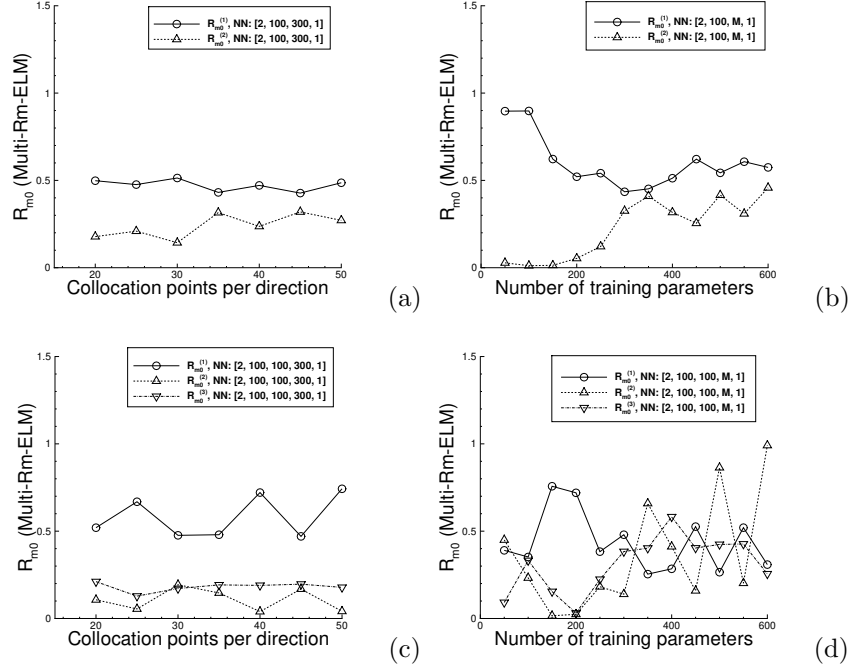


Figure 20: Nonlinear Helmholtz equation (Multi-Rm-ELM): The \mathbf{R}_{m0} components versus the number of collocation points per direction (a,c) and the number of training parameters (b,d), with neural networks having two (a,b) and three (c,d) hidden layers. The network architectures are given in the legends. $Q = 31 \times 31$ in (b,d), varied in (a,c). $M = 300$ in (a,c), varied in (b,d).

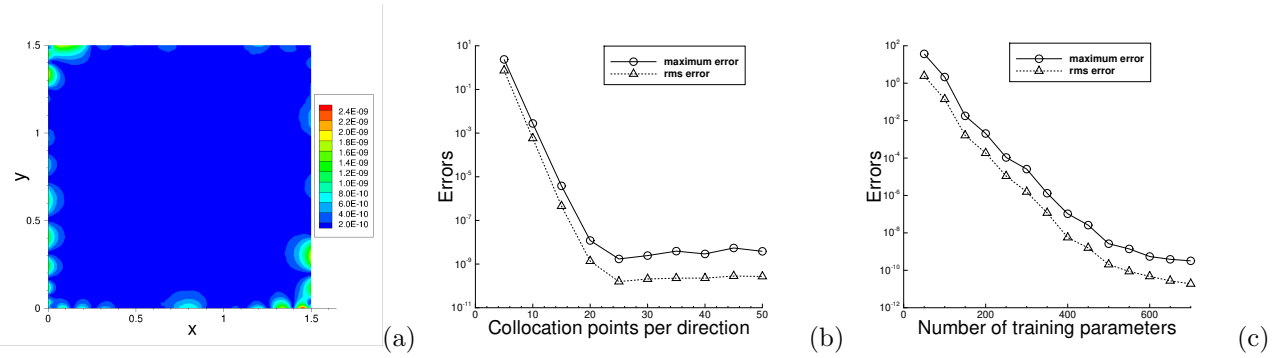


Figure 21: Nonlinear Helmholtz equation (Multi-Rm-ELM): (a) Absolute-error distribution of the Multi-Rm-ELM solution. The maximum/rms errors in the domain versus (b) the number of collocation points per direction, and (c) the number of training parameters. Network architecture: [2, 100, M , 1]. $Q = 31 \times 31$ in (a,c), varied in (b). $M = 500$ in (a,b), varied in (c). $\mathbf{R}_m = (0.55, 0.4)$ in (a,b,c).

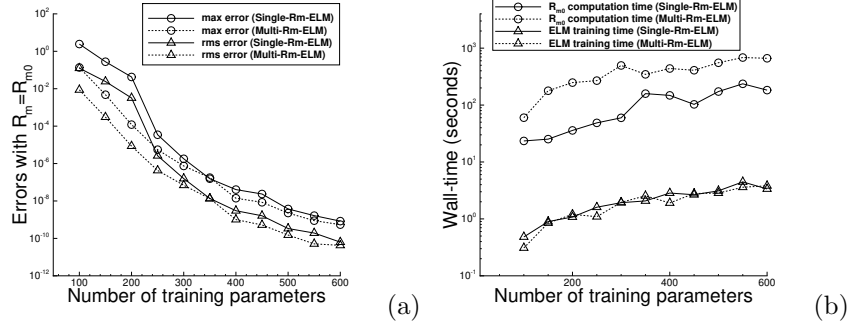


Figure 22: Nonlinear Helmholtz equation: (a) The maximum/rms errors in the domain corresponding to $R_m = R_{m0}$ in Single-Rm-ELM and $\mathbf{R}_m = \mathbf{R}_{m0}$ in Multi-Rm-ELM, versus the number of training parameters (M) in the neural network. (b) The R_{m0}/\mathbf{R}_{m0} computation time and the ELM network training time in Single-Rm-ELM and Multi-Rm-ELM, versus the number of training parameters. Network architecture: $[2, 100, M, 1]$. $Q = 31 \times 31$ in (a,b).

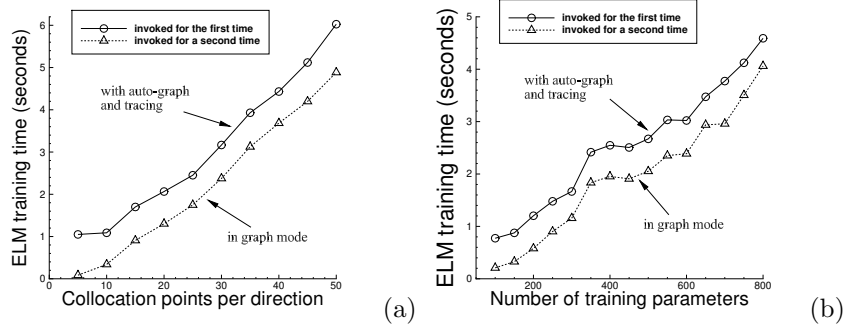


Figure 23: Nonlinear Helmholtz equation (Single-Rm-ELM): ELM network training time versus (a) the number of collocation points per direction and (b) the number of training parameters, obtained with the training routine invoked for the first time or subsequently. The settings and simulation/network parameters here correspond to those of Figures 19(b,c).

provided in Figure 22 with regard to their accuracies and the R_{m0} (\mathbf{R}_{m0}) computation cost. Here the neural network has an architecture $[2, 100, M, 1]$, where M is varied between 100 and 600 in the tests. A fixed set of $Q = 31 \times 31$ uniform collocation points is employed in the domain. For both Single-Rm-ELM and Multi-Rm-ELM, we have employed a population size of 4, the R_m (\mathbf{R}_m) bounds $[0.01, 3]$, and a relative tolerance 0.1 in the differential evolution algorithm. Figure 22(a) shows the maximum/rms errors in the domain of the Single-Rm-ELM and Multi-Rm-ELM solutions obtained with $R_m = R_{m0}$ ($\mathbf{R}_m = \mathbf{R}_{m0}$), as a function of the number of training parameters M . The Multi-Rm-ELM produces a consistently better accuracy than Single-Rm-ELM. Figure 22(b) shows the R_{m0} (\mathbf{R}_{m0}) computation time in Single-Rm-ELM (Multi-Rm-ELM), as well as the ELM network training time for a given R_m (\mathbf{R}_m), as a function of M . The \mathbf{R}_{m0} computation in Multi-Rm-ELM is notably more costly than the R_{m0} computation in Single-Rm-ELM, while the ELM network training cost is essentially the same for given R_m in Single-Rm-ELM and for given \mathbf{R}_m in Multi-Rm-ELM.

Figure 23 illustrates the effect of autograph/tracing and the computation in the graph mode on the ELM network training time for the nonlinear Helmholtz equation. As discussed previously, the Tensorflow Functions for computing the output of the last hidden layer and the associated differential operators are slower when invoked for the first time, because the Tensorflow library would use the autograph/tracing to build the computational graphs. But they run much faster when invoked subsequently. Figures 23(a) and (b) depict the ELM network training time with Single-Rm-ELM, obtained with autograph/tracing (invoked for the first time) or in graph mode (invoked subsequently, no autograph/tracing), as a function of the number

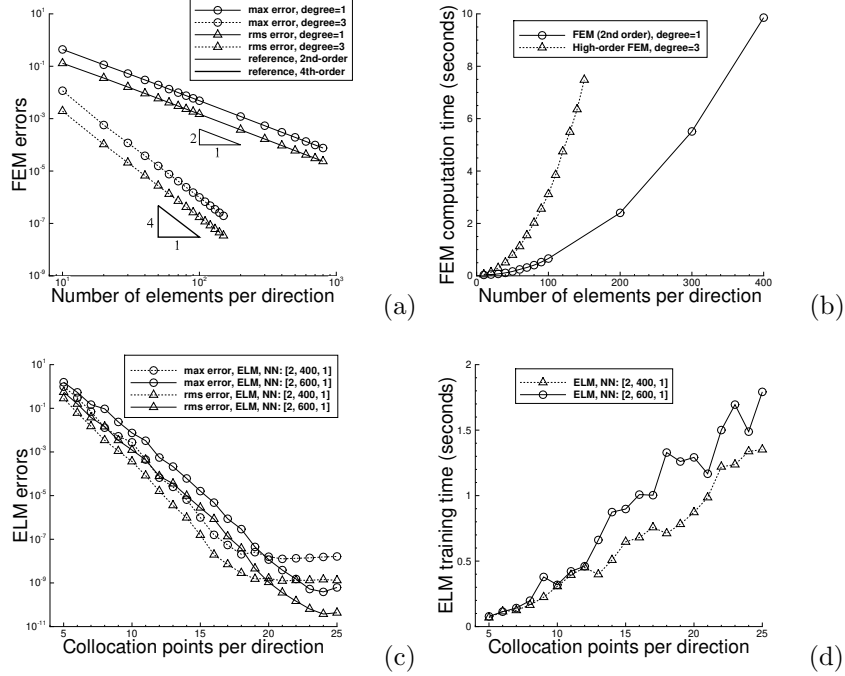


Figure 24: Nonlinear Helmholtz equation (FEM/ELM errors and cost): The numerical errors (a) and the computation time (b) of the classical FEM (degree=1) and the high-order FEM with Lagrange elements of degree 3, versus the number of elements in each direction. The numerical errors (c) and the network training time (d) of the ELM method versus the number of collocation points in each direction. ELM network architecture: $[2, M, 1]$. In (c,d), $R_m = 1.5$ for $M = 400$, and $R_m = 2.1$ for $M = 600$.

of collocation points per direction and the number of training parameters, respectively. The settings and simulation parameters of these two plots correspond to those of the Figures 19(b) and (c), respectively. In the graph mode the ELM network training time is markedly reduced. In the the following comparisons with FEM, the ELM training time refers to the time obtained in the graph mode (no autograph/tracing).

We next compare the computational performance between the ELM method (Single-Rm-ELM configuration) and the classical and high-order FEM for solving the nonlinear Helmholtz equation. With FEM we again use an $N_1 \times N_1$ rectangular mesh (partitioned into $2N_1^2$ triangles), and the nonlinear Helmholtz equation in weak form is solved by the Newton's method from the FEniCS library with a relative tolerance 10^{-12} . We would like to mention an implementation detail concerning the evaluation of the source term and the boundary data in the system (17a)–(17b). When implementing these terms as FEniCS “Expressions”, we have employed the element degree plus 4 as the degree parameter in these Expressions. Note that when solving the Poisson equation in Section 3.3 the degree parameter in the FEniCS Expressions for the source term and the boundary data is set to be the element degree plus one. We find that for nonlinear PDEs (nonlinear Helmholtz equation here, and the Burgers' equation in the next subsection), setting the degree parameter for these FEniCS Expressions to the element degree plus one is not adequate with the high-order elements. When setting it to the element degree plus one, we observe that one cannot quite obtain the expected rate of convergence with the high-order FEM, in particular for cases when the mesh size is not very large. We have tested various cases by setting the degree parameter in these FEniCS Expressions to the element degree plus different extra degrees. We observe that, as the extra degree increases (with the other parameters fixed), the accuracy of the high-order FEM results increases significantly initially, and it levels off as the extra degree increases to 4 and beyond. So in this subsection and the next one (Burgers' equation), we employ the element degree plus 4 as the degree parameter when evaluating the FEniCS Expressions for the source term and the boundary data.

Figure 24 is an overview of the numerical errors of the FEM and ELM and their computational cost

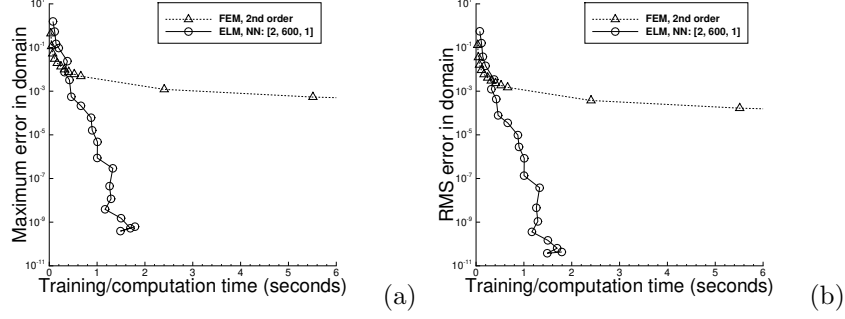


Figure 25: Nonlinear Helmholtz equation (comparison between ELM and classical FEM): The maximum error (a) and the rms error (b) versus the computational cost (ELM network training time, FEM computation time) of the ELM and the classical FEM. The FEM data correspond to those of Figures 24(a,b) with degree=1. The ELM data correspond to those of Figures 24(c,d) with $M = 600$.

(FEM computation time and ELM network training time) for solving the nonlinear Helmholtz equation. Figure 24(a) shows the maximum/rms errors in the domain of the classical FEM (linear elements, degree=1) and the high-order FEM with Lagrange elements of degree=3, as a function of the number of elements in each direction (N_1). The results signify the second-order convergence rate of the classical FEM and the 4th-order convergence rate of the high-order FEM with element degree 3. Figure 24(b) depicts the corresponding computation time versus the number of elements per direction for the classical and high-order FEMs, showing that the cost of the high-order FEM grows much faster than the classical FEM with increasing mesh sizes. Figure 24(c) depicts the maximum/rms errors in the domain of the ELM method (Single-Rm-ELM configuration) as a function of the number of collocation points in each direction. Two neural networks are employed, with architectures $[2, M, 1]$ with $M = 400$ and $M = 600$, respectively. A set of $Q = Q_1 \times Q_1$ uniform collocation points is employed, with Q_1 varied systematically between 5 and 25. In ELM the random hidden-layer coefficients are generated with $R_m = 1.5$ for the neural network with $M = 400$ and $R_m = 2.1$ with $M = 600$, which are close to the R_{m0} obtained with the differential evolution algorithm. The exponential decrease in the ELM errors are unmistakable. Figure 24(d) shows the corresponding ELM network training time as a function of the number of collocation points. Here the ELM training time refers to the time obtained in the graph mode (without autograph/tracing). One can observe that, as the number of collocation points increases, the growth in the ELM training time is nearly linear.

Figure 25 compares the computational performance of the ELM and the classical FEM (2nd-order, linear elements). It plots the maximum error (plot (a)) and the rms error (plot (b)) in the domain of the ELM (and the classical FEM) versus the ELM network training time (resp. the FEM computation time). The FEM data correspond to those in Figures 24(a,b) with degree=1, and the ELM data here correspond to those in Figures 24(c,d) with $M = 600$ in the neural network. The ELM far outperforms the classical FEM in almost all cases, achieving a considerably better accuracy with the same computational cost/budget or inducing a considerably smaller cost to achieve the same accuracy. The exception is in a range of very small problem sizes (FEM mesh size smaller than around 70×70 , ELM collocation points less than around 10×10 , error level above around $5 \times 10^{-3} \sim 10^{-2}$, wall time less than around 0.3 seconds), where the ELM performance and the FEM performance are close, with the FEM a little better.

A comparison between ELM and the high-order FEM is provided in Figure 26 for solving the nonlinear Helmholtz equation. We have again performed the h-type refinement (fix the element degree, vary the mesh size) and the p-type refinement (fix the mesh size, vary the element degree between 1 and 7) with high-order FEM. Figures 26(a) and (b) depict the maximum and rms errors, respectively, of the high-order FEM under the h-type refinements versus the FEM computation time. The FEM data for the element degree=3 in these plots correspond to those in Figures 24(a,b) with degree=3. Figures 26(c) and (d) depict the maximum and rms errors of the high-order FEM under the p-type refinements versus the FEM computation time. These four plots also include the maximum and rms errors of the ELM method versus the ELM network training time. The ELM data here correspond to those in Figures 24(c,d) for the two neural networks.

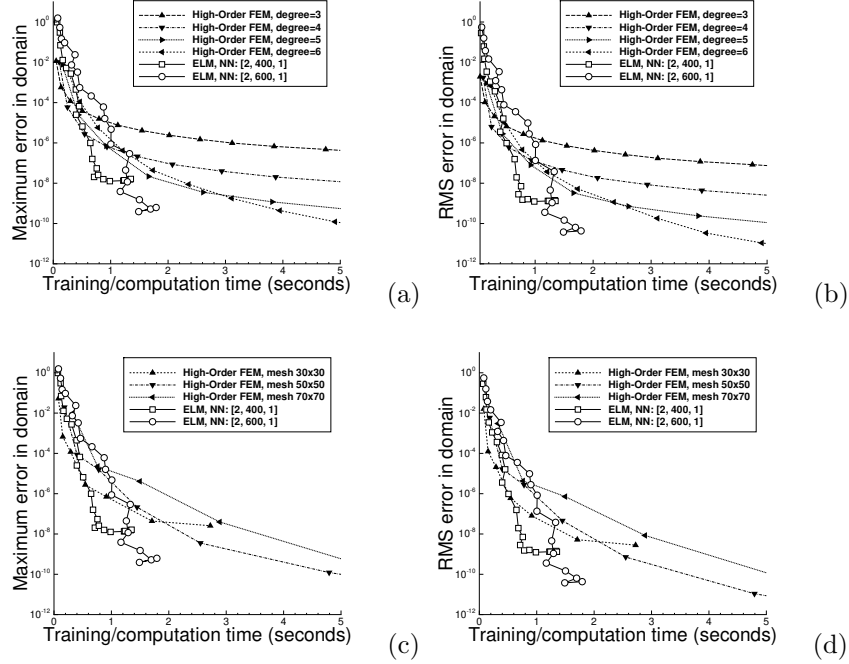


Figure 26: Nonlinear Helmholtz equation (comparison between ELM and high-order FEM): The maximum error (a,c) and the rms error (b,d) in the domain versus the computational cost (ELM training time, FEM computation time) between ELM and high-order FEM with various element degrees. In (a,b) the number of elements per direction in the FEM mesh is varied systematically for each given element degree. In (c,d) the degree of the Lagrange elements is varied systematically for each given mesh size. The FEM data of degree 3 in (a,b) correspond to those of Figures 24(a,b) with degree 3. The ELM data in (a,b,c,d) correspond to those of Figures 24(c,d).

We can make the following observations from Figure 26. The ELM method outperforms the high-order FEM as the problem size becomes larger (larger FEM mesh size under fixed element degree, or larger element degree under fixed mesh size; larger set of ELM collocation points). With smaller problem sizes (smaller FEM mesh size under fixed element degree, or smaller element degree under fixed mesh size; smaller set of ELM collocation points), the computational performances of ELM and high-order FEM are comparable, with the high-order FEM being slightly better. These observations with the nonlinear Helmholtz equation here are consistent with what has been observed for the Poisson equation (linear) in the previous subsection.

3.5 Viscous Burgers' Equation

We next use another nonlinear example, the viscous Burgers' equation, to test the method for computing the optimal R_m (\mathbf{R}_m) and also compare the computational performance of the ELM method with the classical and high-order FEMs. A seed value of 100 has been employed for the random number generators in Tensorflow and numpy for all the numerical tests in this subsection.

We consider the spatial-temporal domain, $\Omega = \{(x, t) \mid 0 \leq x \leq 2, 0 \leq t \leq 5\}$, and the following initial-boundary value problem with the viscous Burgers' equation on Ω ,

$$\frac{\partial u}{\partial t} + u \frac{\partial u}{\partial x} - \nu \frac{\partial^2 u}{\partial x^2} = f(x, t), \quad (19a)$$

$$u(0, t) = g_1(t), \quad u(2, t) = g_2(t), \quad (19b)$$

$$u(x, 0) = h(x), \quad (19c)$$

where $\nu = 0.01$, $u(x, t)$ is the field solution to be sought, $f(x, t)$ is a prescribed source term, g_1 and g_2 are the

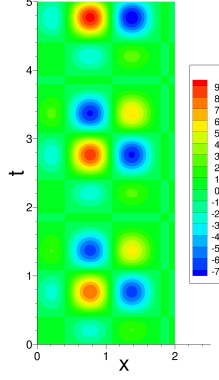


Figure 27: Burgers' equation: distribution of the exact solution.

prescribed Dirichlet boundary condition, and h denotes the initial distribution. We choose the source term and the boundary/initial distributions such that the following manufactured function solves the system (19),

$$u(x, t) = \left(1 + \frac{x}{20}\right) \left(1 + \frac{t}{20}\right) \left[\frac{3}{2} \cos\left(\pi x + \frac{7\pi}{20}\right) + \frac{27}{20} \cos\left(2\pi x - \frac{3\pi}{5}\right) \right] \left[\frac{3}{2} \cos\left(\pi t + \frac{7\pi}{20}\right) + \frac{27}{20} \cos\left(2\pi t - \frac{3\pi}{5}\right) \right]. \quad (20)$$

Figure 27 illustrates the distribution of this function in the spatial-temporal plane.

We employ the ELM method (Single-Rm-ELM and Multi-Rm-ELM configurations), together with the block time marching scheme (see Remark 2.7), to solve the system (19). The input layer of the neural network contains two nodes, representing x and t . The linear output layer contains a single node, representing the solution $u(x, t)$. The network contains one or multiple hidden layers, with the Gaussian activation function for all the hidden nodes. The random hidden-layer coefficients are set according to the Single-Rm-ELM or Multi-Rm-ELM configurations from Section 2.

We partition the spatial-temporal domain into a number of windows in time (time blocks), and solve the problem on the time blocks individually and successively [10]. On each time block, the ELM network is trained by the NLLSQ-perturb method [10]. After one time block is computed, its field solution evaluated at the last time instant is used as the initial condition for the computation of the next time block. As discussed in Remark 2.7, we compute the R_{m0} and \mathbf{R}_{m0} by the differential evolution algorithm only on the first time block, and we turn off the random perturbations and the associated subiterations in the nonlinear least squares method (NLLSQ-perturb) during the R_{m0} (\mathbf{R}_{m0}) computation.

The crucial simulation parameters for this problem include the time block size (or the number of time blocks), the number of training parameters M (width of last hidden layer in network), the set of $Q = Q_1 \times Q_1$ uniform collocation points on each time block, and the maximum magnitude R_m (or \mathbf{R}_m) of the random coefficients. We employ 20 uniform time blocks on the domain Ω , resulting in a time block size 0.25. Therefore, the R_{m0} and \mathbf{R}_{m0} are computed on the first time block, i.e. by using the spatial-temporal domain $\Omega_1 = \{(x, t) \mid x \in [0, 2], t \in [0, 0.25]\}$.

We first consider the Single-Rm-ELM configuration, and Figure 28 illustrates the optimum R_{m0} obtained with the differential evolution algorithm for the Burgers' equation. In these tests the computational domain is the spatial-temporal domain of the first time block Ω_1 , and we employ neural networks with one to three hidden layers. The number of training parameters is either fixed at $M = 300$ or varied systematically. The set of $Q = Q_1 \times Q_1$ uniform collocation points is either fixed at $Q_1 = 31$ or varied systematically.

Figure 28(a) depicts the optimum R_{m0} as a function of the number of collocation points per direction Q_1 , for three neural networks with the same $M = 300$ but different depth. Figures 28(b) and (c) both depict the R_{m0} as a function of the number of training parameters M , but for neural networks with different configurations. The plot (b) is for three neural networks with different depths, and the plot (c) is for three neural networks with the same depth but different widths for the preceding hidden layers. These results are

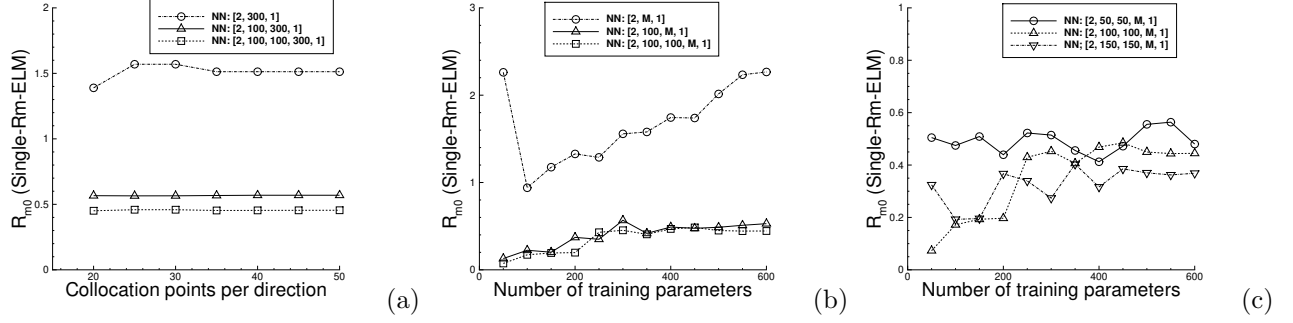


Figure 28: Burgers' equation (Single-Rm-ELM): The optimum R_{m0} versus (a) the number of collocation points per direction and (b) the number of training parameters, with neural networks of different depth. (c) R_{m0} versus the number of training parameters with neural networks having the same depth but different widths. Domain: $\Omega_1 = [0, 2] \times [0, 0.25]$. $Q = 31 \times 31$ in (b,c), varied in (a). $M = 300$ in (a), varied in (b,c). The network architectures are given in the legends.

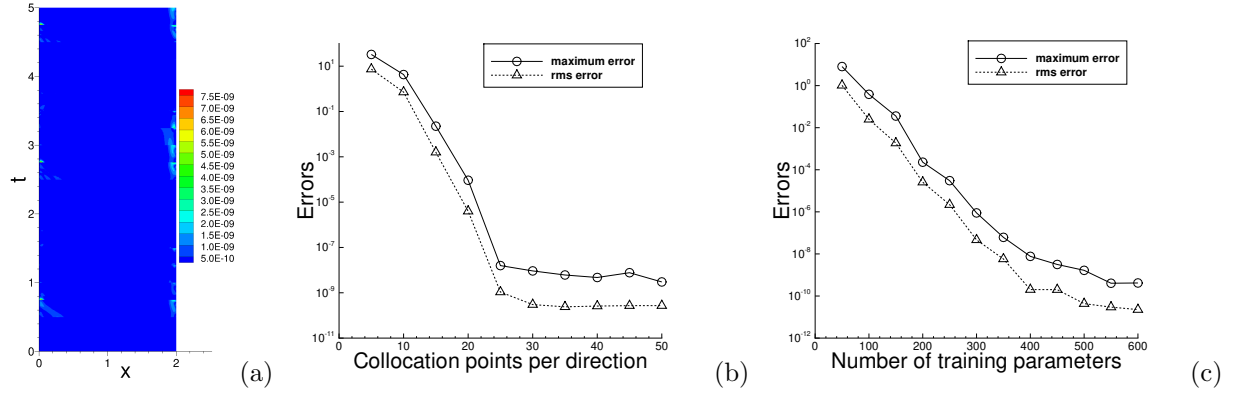


Figure 29: Burgers' equation (Single-Rm-ELM): (a) Absolute-error distribution of the Single-Rm-ELM solution on Ω . The maximum/rms errors on Ω versus (b) the number of collocation points per direction on each time block, and (c) the number of training parameters. Domain: Ω , with 20 time blocks in block time marching. Network architecture: $[2, M, 1]$. $Q = 31 \times 31$ in (a,c), varied in (b). $M = 400$ in (a,b), varied in (c). $R_m = 2.0$ in (a,b,c).

obtained with a population size of 6, the R_m bounds $[0.01, 3]$, and a relative tolerance 0.1 in the differential evolution algorithm. The settings and simulation parameters for each plot are provided in the figure caption.

The R_{m0} characteristics shown by Figure 28 are consistent with those observed from previous subsections. For instance, R_{m0} is generally not sensitive to the number of collocation points in the domain, especially with more than one hidden layers in the neural network. With a single hidden layer in the neural network, R_{m0} has a notable dependence on the number of training parameters M , and tends to increase with increasing M (Figure 28(b)). With two or more hidden layers in the neural network, R_{m0} only weakly depends on M . R_{m0} tends to decrease with increasing depths in the neural network or increasing widths of the preceding hidden layers. When the number of hidden layers increases from one to two, the reduction in R_{m0} is quite pronounced. Beyond two hidden layers, on the other hand, there is only a slight reduction in R_{m0} as the number of hidden layers increases.

Figure 29 illustrates the solution accuracy of the Single-Rm-ELM configuration. The computational domain here is the entire spatial-temporal domain Ω ($0 \leq t \leq 5$), and we employ 20 time blocks in the block time marching scheme, as mentioned before. The neural network has an architecture $[2, M, 1]$, where M is either fixed at $M = 400$ or varied systematically. A set of $Q = Q_1 \times Q_1$ uniform collocation points is employed on each time block, with Q_1 either fixed at 31 or varied systematically. We employ a fixed

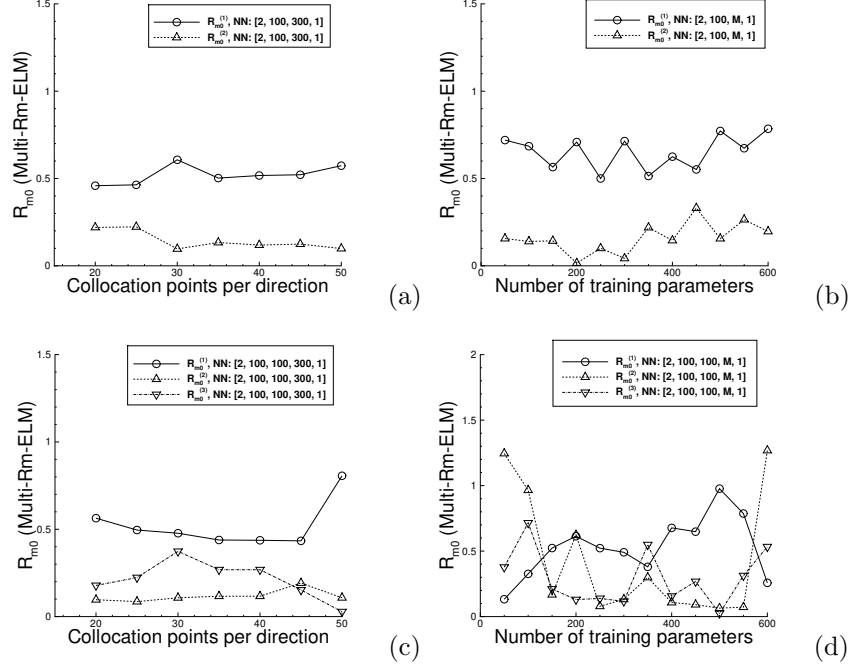


Figure 30: Burgers' equation (Multi-Rm-ELM): The optimum \mathbf{R}_{m0} versus the number of collocation points per direction (a,c) and the number of training parameters (b,d), with neural networks having two (a,b) and three (c,d) hidden layers. The network architectures are given in the legends. Computational domain: Ω_1 ($t \in [0, 0.25]$). $Q = 31 \times 31$ in (b,d), varied in (a,c). $M = 300$ in (a,c), varied in (b,d).

$R_m = 2.0$ in all these tests, which is close to the R_{m0} obtained from the differential evolution algorithm corresponding to $M = 500$ and $Q = 31 \times 31$. Figure 29(a) shows the distribution of the absolute error of the Single-Rm-ELM solution, signifying a high accuracy with the maximum error on the order 10^{-9} in the entire spatial-temporal domain. Figures 29(b) and (c) depict the maximum/rms errors in the overall domain as a function of Q_1 and M , respectively, showing the exponential convergence in the numerical errors (before saturation). The simulation parameters for each plot are provided in the figure caption.

Let us next look into the Multi-Rm-ELM configuration for solving the Burgers' equation. The characteristics of the optimum \mathbf{R}_{m0} are illustrated in Figure 30. The computational domain in these tests is the spatial-temporal domain Ω_1 ($t \in [0, 0.25]$). We have considered two types of neural networks, whose architectures are given by $[2, 100, M, 1]$ and $[2, 100, 100, M, 1]$, where M is fixed at 300 or varied systematically. A uniform set of $Q = Q_1 \times Q_1$ collocation points is employed in the domain, where Q_1 is fixed at 31 or varied systematically. We employ a population size of 6, the bounds $[0.01, 3]$ for all the \mathbf{R}_m components, and a relative tolerance 0.1 in the differential evolution algorithm for these tests.

Figures 30(a) and (b) depict the optimum $\mathbf{R}_{m0} = (R_{m0}^{(1)}, R_{m0}^{(2)})$ as a function of Q_1 and M , respectively, for the neural networks with two hidden layers. Figures 30(c) and (d) depict the corresponding components of the optimum $\mathbf{R}_{m0} = (R_{m0}^{(1)}, R_{m0}^{(2)}, R_{m0}^{(3)})$ as a function of Q_1 and M for the neural networks with three hidden layers. Overall, the relations of \mathbf{R}_{m0} versus Q_1 and M appear to be quite irregular. The relation between \mathbf{R}_{m0} and Q_1 seems less irregular, and the dependence appears generally not quite strong. On the other hand, the change in M appears to affect the \mathbf{R}_{m0} components more strongly, especially with increasing number of hidden layers in the neural network (see Figure 30(d)). These characteristics are similar to those observed in previous subsections with Multi-Rm-ELM for linear and nonlinear problems.

The solution accuracy of the Multi-Rm-ELM configuration is illustrated in Figure 31. The computational domain in this set of tests is the spatial-temporal domain Ω ($t \in [0, 5]$), which is partitioned into 25 time blocks (block size 0.2 in time) in the block time marching scheme with Multi-Rm-ELM. The neural network architecture is given by $[2, 100, M, 1]$, with M fixed at 400 or varied systematically. A uniform set of $Q =$

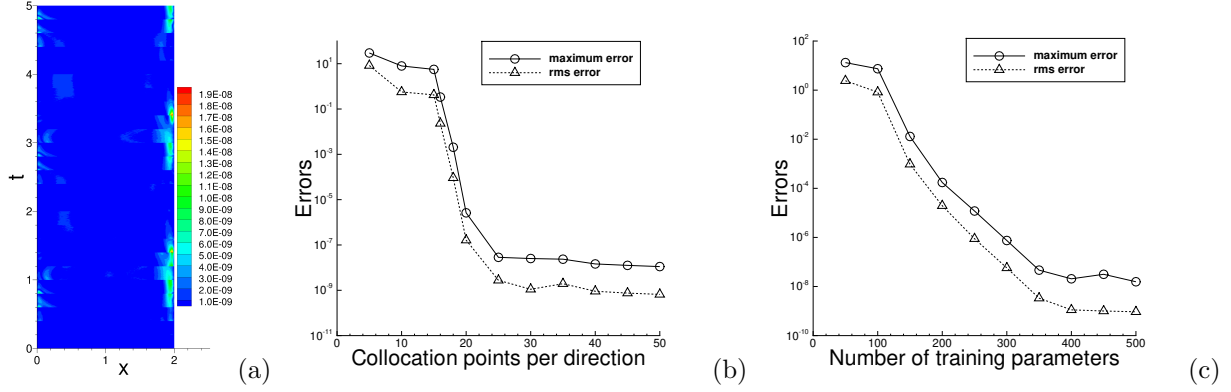


Figure 31: Burgers' equation (Multi-Rm-ELM): (a) Absolute-error distribution of the Multi-Rm-ELM solution in the spatial-temporal domain. The maximum/rms errors on Ω versus (b) the number of collocation points per direction in each time block, and (c) the number of training parameters. Computational domain: Ω , with 25 time blocks in block time marching. Network architecture: $[2, 100, M, 1]$. $Q = 31 \times 31$ for each time block in (a,c), varied in (b). $M = 400$ in (a,b), varied in (c). $\mathbf{R}_m = (0.625, 0.145)$ in (a,b,c).

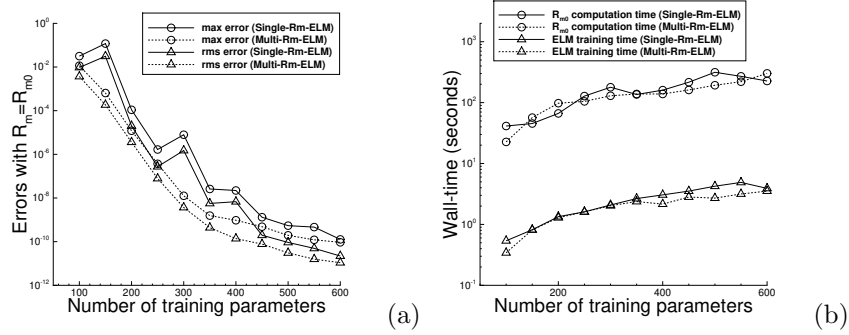


Figure 32: Burgers' equation: (a) The maximum/rms errors corresponding to $R_m = R_{m0}$ in Single-Rm-ELM and $\mathbf{R}_m = \mathbf{R}_{m0}$ in Multi-Rm-ELM, versus the number of training parameters (M). (b) The R_{m0} (or \mathbf{R}_{m0}) computation time and the ELM network training time in Single-Rm-ELM and Multi-Rm-ELM, versus the number of training parameters. Computational domain: Ω_1 ($t \in [0, 0.25]$). Network architecture: $[2, 100, M, 1]$. $Q = 31 \times 31$ in (a,b).

$Q_1 \times Q_1$ collocation points is employed on each time block, where Q_1 is fixed at 31 or varied systematically. We employ a fixed $\mathbf{R}_m = (0.645, 0.145)$ in these tests, which is close to the \mathbf{R}_{m0} obtained with the differential evolution algorithm corresponding to $M = 400$ and $Q = 31 \times 31$. Figure 31(a) shows the distribution of the absolute error of the Multi-Rm-ELM solution on the entire spatial-temporal domain. The results signify a high accuracy, with a maximum error on the order 10^{-8} in the overall domain. Figures 31(b) and (c) depict the maximum error and the rms error in the overall domain of the Multi-Rm-ELM solution as a function of Q_1 and M . The errors generally appear to decrease exponentially or nearly exponentially with increasing number of collocation points or training parameters. But the relation is not that regular. For example, in Figure 31(b) as the collocation points increase from 5×5 to 15×15 , there is little decrease in the errors. However, once beyond that point, there is a sharp exponential decrease in the errors (before saturation).

A comparison between Single-Rm-ELM and Multi-Rm-ELM with regard to their accuracies and the cost for computing R_{m0}/\mathbf{R}_{m0} is provided in Figure 32. The computational domain is the spatial-temporal domain Ω_1 ($t \in [0, 0.25]$). The neural network has an architecture $[2, 100, M, 1]$ in this group of tests, where M is varied systematically. The random hidden-layer coefficients are set based on the Single-Rm-ELM or Multi-Rm-ELM configurations. A fixed set of $Q = 31 \times 31$ uniform collocation points is employed. Figure 32(a) shows the maximum/rms errors in the domain versus the number of training parameters M , corresponding

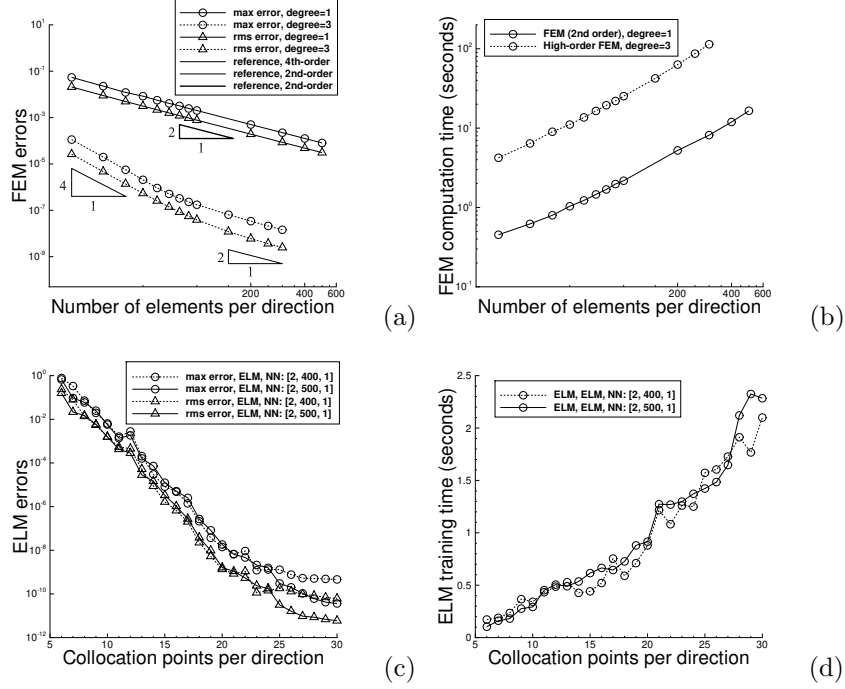


Figure 33: Burgers' equation: The numerical errors (a) and the computation time (b) of the classical FEM (2nd-order, degree=1) and the high-order FEM with Lagrange elements of degree 3, versus the number of elements in each direction. In the FEM tests, as the number of elements increases, the time step size (Δt) is decreased proportionately. The numerical errors (c) and the network training time (d) of the ELM method versus the number of collocation points in each direction of the time block. Computational domain: Ω_1 ($t \in [0, 0.25]$). The network architectures are given in the legends.

to $R_m = R_{m0}$ in Single-Rm-ELM and $\mathbf{R}_m = \mathbf{R}_{m0}$ in Multi-Rm-ELM. Here when computing R_{m0} and \mathbf{R}_{m0} we have employed a population size of 6, the bounds $[0.01, 3]$, and a relative tolerance 0.1 in the differential evolution algorithm for both Single-Rm-ELM and Multi-Rm-ELM. One can observe that Multi-Rm-ELM leads to consistently more accurate results than Single-Rm-ELM. Figure 32(b) shows the corresponding cost for computing the R_{m0}/\mathbf{R}_{m0} in Single-Rm-ELM and Multi-Rm-ELM, as well as the ELM network training time with given R_m/\mathbf{R}_m , as a function of M . The R_{m0} computation cost in Single-Rm-ELM and the \mathbf{R}_{m0} computation cost in Multi-Rm-ELM appear comparable for the Burgers' equation. The cost for computing the R_{m0}/\mathbf{R}_{m0} is markedly higher than the ELM network training time for a given R_m or \mathbf{R}_m .

Let us next compare the ELM method (Single-Rm-ELM configuration) with the FEM (classical and high-order FEMs) for solving the Burgers' equation. The computational domain is the spatial-temporal domain Ω_1 ($t \in [0, 0.25]$) in the following tests.

With FEM, we employ a second-order semi-implicit type time integration scheme to solve the Burgers' equation (see [10]). We discretize the time derivative term in (19a) by the second-order backward differentiation formula (BDF2), treat the diffusion term implicitly, and treat the nonlinear term explicitly. The temporally semi-discretized equation in weak form is then solved in space by the classical (2nd-order) FEM or high-order FEM with Lagrange elements, which are implemented using the FEniCS library with uniform 1D interval mesh. The FEM simulation parameters include the time step size Δt (or the number of time steps), the number of elements in space, and the element degree for high-order FEM. In the FEM tests, we vary the number of elements systematically and simultaneously vary the number of time steps accordingly, so that the Δt and the element size is increased or decreased proportionately. The element degree is also varied with the high-order FEM. As mentioned in Section 3.4, the degree parameter in the FEniCS "Expressions" for the source term and the boundary/initial data in (19) is set to be the element degree plus 4 with FEM.

With ELM, we employ one time block in the spatial-temporal domain Ω_1 . We consider two neural

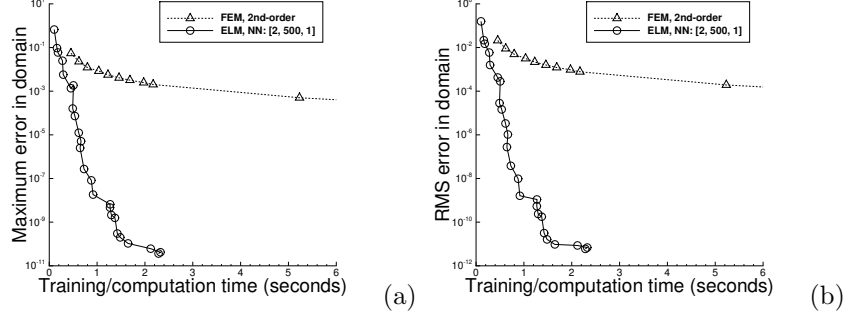


Figure 34: Burgers' equation (comparison between ELM and classical FEM): The maximum errors (a) and the rms errors (b) in the spatial-temporal domain versus the computational cost (ELM training time, FEM computation time) between ELM and the classical FEM. The FEM data correspond to those in Figures 33(a,b) with degree=1. The ELM data correspond to those in Figures 33(c,d) with $M = 500$.

networks with the architecture $[2, M, 1]$ with $M = 400$ and $M = 500$, respectively. A fixed $R_m = 2.0$ is used to generate the random hidden-layer coefficients. We employ a uniform set of $Q = Q_1 \times Q_1$ collocation points on the spatial-temporal domain Ω_1 , where Q_1 is varied systematically in the tests.

Figure 33 provides an overview of the errors and the computational cost of the FEM and the ELM for solving the Burgers' equation. Figures 33(a) and (b) show the maximum/rms errors in Ω_1 , and the computation time, of the classical FEM (2nd-order, degree=1) and the high-order FEM with Lagrange elements of degree=3, as a function of the number of elements in the mesh. Since the element size and the time step size Δt are varied proportionately, these plots equivalently show the relations of the errors (or computation time) versus Δt . With the classical FEM, the number of elements varies between 20 and 500, and Δt is varied proportionately between $1.25E - 3$ and $5.0E - 5$ in these data. With the high-order FEM of degree=3, the number of elements varies between 20 and 300, and Δt is varied proportionately between $1.25E - 4$ and $8.33E - 6$. We clearly observe a second-order convergence rate of the classical FEM with respect to the number of elements, and also with respect to Δt . With Lagrange elements of degree 3, we observe a 4th-order convergence rate initially (when the number of elements is not large), which then transitions to a second-order convergence rate when the number of elements increases beyond a certain point. The observed change in the convergence rate with high-order FEM is due to the interplay and the dominance of the spatial truncation error or the temporal truncation error in different regimes. When the spatial error dominates, what one observes is the actual spatial convergence rate (4th-order with element degree 3). When the temporal error dominates, on the other hand, what one observes is the second-order convergence rate with respect to Δt , because the spatial error becomes insignificant compared with the temporal error in this case. Figure 33(b) signifies that computational cost of the high-order FEM is markedly larger than that of the classical FEM.

Figures 33(c) and (d) depict the maximum/rms errors and the network training time of the ELM as a function of the number of collocation points in each direction (Q_1) with the two neural networks. Here the ELM training time is the time obtained in the graph mode (no autograph/tracing). We observe the familiar exponential decrease in the ELM errors. The plot (d) indicates that the ELM network training time grows nearly linearly with increasing number of collocation points.

Figure 34 compares the computational performance between the ELM method and the classical FEM for the Burgers' equation. The two plots show the maximum errors and the rms errors in the overall spatial-temporal domain of the ELM and classical FEM solutions versus their computational cost (ELM network training time, FEM computation time). The FEM data here correspond to those in Figures 33(a,b) with degree=1, and the ELM data correspond to those in Figures 33(c,d) with the neural network architecture $[2, 500, 1]$. One can observe that the ELM method consistently and far outperforms the classical FEM.

Figure 35 is a comparison of the computational performance between the ELM and the high-order FEM for solving the Burgers' equation. The computational domain here is the spatial-temporal domain Ω_1 ($t \in [0, 0.25]$). Two sets of FEM tests are conducted here, in both of which the element size and the time step

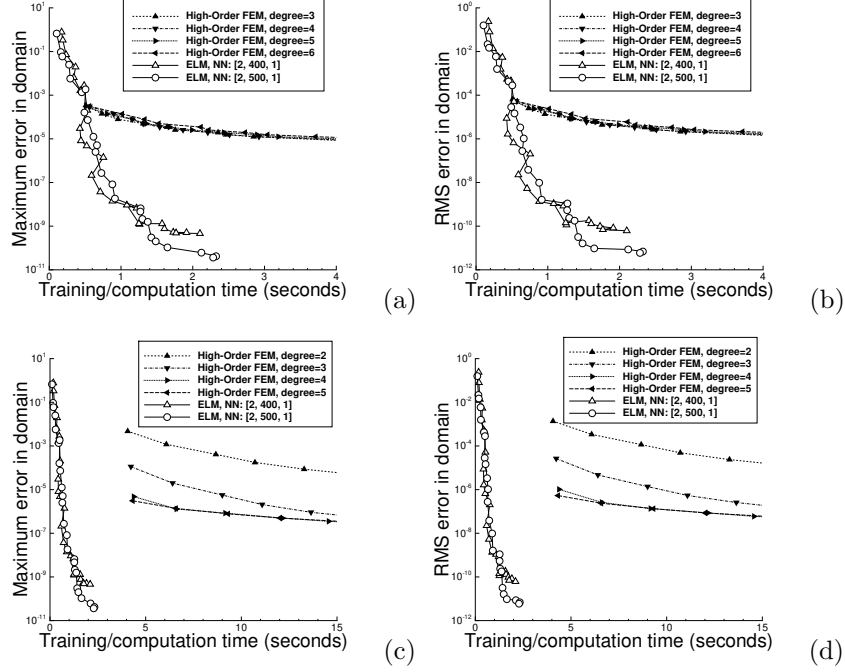


Figure 35: Burgers' equation (comparison between ELM and high-order FEM): The maximum error (a,c) and the rms error (b,d) in the spatial-temporal domain versus the computational cost (ELM training time, FEM computation time) between ELM and high-order FEM. Computational domain: Ω_1 ($t \in [0, 0.25]$). The ELM data correspond to those in Figures 33(c,d). In the FEM tests, the element size and the time step size (Δt) are decreased simultaneously and proportionately for each given element degree. In (a,b), the number of FEM elements varies between 20 and 500, and Δt varies between $1.25E - 3$ and $5E - 5$. In (c,d), the number of FEM elements varies between 20 and 100, and Δt varies between $1.25E - 4$ and $2.5E - 5$. The FEM data with degree=3 in (c,d) correspond to a portion of the data in Figures 33(a,b) with degree=3.

size (Δt) are reduced simultaneously and proportionately for a given element degree. In the first set of tests, the number of elements vary between 20 and 500, and the time step size varies between $\Delta t = 1.25E - 3$ and $\Delta t = 5.0E - 5$ accordingly. In the second set, the number of elements vary between 20 and 100, and the time step size varies between $\Delta t = 1.25E - 4$ and $\Delta t = 2.5E - 5$ accordingly. The ELM data correspond to those given in Figures 33(c,d).

Figures 35(a) and (b) show the maximum errors and the rms errors, respectively, of the high-order FEM and the ELM solutions in the spatial-temporal domain versus the FEM computation time and the ELM network training time for the first set of FEM tests. We observe that the FEM curves corresponding to different element degrees essentially overlap with one another. This is because in this set of tests the Δt is relatively large and the temporal truncation error dominates. So in this case increasing the element degree barely affects the total FEM error. The data in Figures 35(a,b) demonstrate that the ELM consistently outperforms the high-order FEM, and by a considerable margin as the problem size increases.

Figures 35(c) and (d) show the maximum and rms errors of the high-order FEM versus the computation time for the second set of FEM tests, together with the ELM errors versus the ELM training time. We can observe that the FEM error generally decreases as the element degree increases (e.g. from 2 to 3 and 4), and that the FEM error remains essentially the same as the element degree increases to 4 and beyond. This is because the Δt is smaller here than in the first set of FEM tests, and so the spatial truncation error dominates the FEM total error, at least with the smaller element degrees. As the element degree increases, the spatial truncation error is reduced rapidly and the temporal truncation error gradually becomes dominant. At this point, further increase in the FEM element degree will not notably affect the total FEM error. Because of the smaller Δt values in the second set of FEM tests, a significantly larger number of time steps need to be

computed in the FEM simulations, resulting in an overall increased FEM computation time. We can observe from Figures 35(c,d) that the ELM way outperforms the high-order FEM for this set of tests.

The above comparisons show that the ELM method combined with block time marching is effective and efficient for solving time dependent PDEs. It is considerably more efficient than the FEM (classical and high-order FEMs) combined with the commonly-used second-order time stepping scheme, in terms of the accuracy and the incurred computational cost. These comparisons are conducted on a relatively small temporal domain ($t \in [0, 0.25]$). When the temporal dimension of the spatial-temporal domain increases (i.e. for longer-time simulations), the advantage of the ELM combined with block time marching becomes even more prominent.

4 Concluding Remarks

In extreme learning machines (ELM) the hidden-layer coefficients of the neural network are pre-set to uniform random values generated on the interval $[-R_m, R_m]$, where the maximum magnitude R_m of the random coefficients is a user-provided constant (hyperparameter), and the output-layer coefficients are trained by a linear or nonlinear least squares computation [10]. More accurate ELM results have been observed to be associated with a range of moderate values for R_m (see [10]). In the current paper, we have presented a method for computing the optimal or near-optimal value for the R_m constant for solving partial differential equations (PDE). The presented method is based on the differential evolution algorithm, and seeks the optimal R_m by minimizing the norm of the residual vector of the linear or nonlinear algebraic system that results from the ELM representation of the PDE solution and that corresponds to the ELM least squares solution to the system. This method amounts to a pre-processing procedure. It determines a near optimal value for R_m , which can be used in ELM for solving linear or nonlinear PDEs. In practice, we observe that any value in a neighborhood of the returned R_{m0} from the method can be used in the ELM simulation and leads to comparable accuracy. This is because, as shown in [10], there is usually a range of R_m values that lead to good accuracy with ELM.

We have investigated two configurations in ELM for setting the random hidden-layer coefficients, Single-Rm-ELM and Multi-Rm-ELM. The Single-Rm-ELM configuration corresponds to the conventional ELM, in which the weight/bias coefficients for all the hidden layers of the neural network are assigned to random values generated on $[-R_m, R_m]$, with a single R_m constant. In the Multi-Rm-ELM configuration, the weight/bias coefficients in the l -th hidden layer, $1 \leq l \leq L - 1$ with $(L - 1)$ denoting the total number of hidden layers, are set to random values generated on $[-R_m^{(l)}, R_m^{(l)}]$. Therefore, the maximum magnitudes of the random coefficients in different hidden layers may be different in Multi-Rm-ELM, and they are characterized by the vector $\mathbf{R}_m = (R_m^{(1)}, R_m^{(2)}, \dots, R_m^{(L-1)})$.

We have computed the optimal R_m in Single-Rm-ELM and the optimal \mathbf{R}_m in Multi-Rm-ELM using the method developed here for a number of linear and nonlinear PDEs. We have the following observations about the Single-Rm-ELM and Multi-Rm-ELM and their respective optimum R_{m0} and \mathbf{R}_{m0} :

- The optimum R_{m0} of Single-Rm-ELM is largely independent of the number of collocation points. R_{m0} only weakly depends on the number of training parameters for neural networks with two or more hidden layers. For neural networks with a single hidden layer, the dependence of R_{m0} on the number of training parameters (M) is stronger, and R_{m0} tends to increase with increasing M (when M is not very small).
- R_{m0} generally decreases with increasing number of hidden layers in the neural network. There is a fairly large drop in R_{m0} from a single hidden layer to two hidden layers. Beyond two hidden layers, the decrease in R_{m0} is only slight and can oftentimes be negligible as the number of hidden layers further increases.
- R_{m0} has only a very weak (oftentimes negligible) dependence on the number of nodes in the hidden layers preceding the last hidden layer. R_{m0} tends to decrease slightly with increasing width of the preceding hidden layers.
- The optimum \mathbf{R}_{m0} of Multi-Rm-ELM tends to exhibit a relationship that is not quite regular with respect to the ELM simulation parameters. However, the trend exhibited by \mathbf{R}_{m0} appears reminiscent

of what has been observed about the optimum R_{m0} of Single-Rm-ELM. For example, \mathbf{R}_{m0} depends only weakly on (or nearly independent of) the number of collocation points, and appears to generally increase with increasing number of training parameters.

- The Multi-Rm-ELM configuration with $\mathbf{R}_m = \mathbf{R}_{m0}$ leads to consistently more accurate simulation results than the Single-Rm-ELM configuration with $R_m = R_{m0}$, under otherwise identical conditions. On the other hand, the \mathbf{R}_{m0} computation cost in Multi-Rm-ELM is generally higher than the R_{m0} computation cost in Single-Rm-ELM.

We have made several improvements to the implementation of the ELM method in the current work. The most crucial change lies in the adoption of a forward-mode auto-differentiation for computing the differential operators associated with the output fields of the last hidden layer of the neural network. This is implemented using the “ForwardAccumulator” in Tensorflow. In contrast, these differential operators were computed by the default reverse-mode auto-differentiation (“GradientTape”) of Tensorflow in the previous work [10]. These improvements result in a significant boost to the computational performance of ELM.

Another aspect of the current contribution is a systematic comparison of the computational performance between the current ELM method and the classical and high-order finite element methods (FEM) for solving linear and nonlinear PDEs. The ELM method employs the improved implementation and the near optimal R_m obtained from the differential evolution algorithm. The classical FEM (second-order, linear elements) and the high-order FEM are implemented based on the FEniCS library by employing the Lagrange elements of degree one or higher degrees. By looking into the ELM/FEM accuracy and their computational cost (FEM computation time, ELM network training time) for a number of linear/nonlinear PDEs, we have the following observations:

- For stationary (i.e. time-independent) PDEs, the ELM far outperforms the classical FEM if the problem size is not very small. For very small problem sizes (small FEM mesh, small number of ELM training collocation points), the computational performance of the ELM and the classical FEM is close, with the classical FEM a little better.
- For stationary PDEs, there is a crossover point in the relative performance between ELM and the high-order FEM with respect to the problem size (FEM mesh size or element degree, ELM collocation points). For smaller problem sizes (smaller FEM mesh in h-type refinements or smaller element degree in p-type refinement; smaller number of ELM collocation points), the ELM and high-order FEM are close in computational performance, with the high-order FEM appearing slightly better. As the problem size becomes larger, the ELM markedly outperforms the high-order FEM.
- For time-dependent PDEs, the ELM method combined with the block time marching scheme consistently and significantly outperforms both the classical and the high-order FEMs (combined with a time-stepping scheme).

These performance comparisons demonstrate that the neural network-based ELM method is computationally competitive compared with not only the classical second-order FEM but also the high-order FEM based on high-order polynomials. The ELM exceeds the classical FEM by a considerable margin in terms of computational performance. The ELM method delivers a comparable performance to high-order FEM for smaller problem sizes. For larger problem sizes, the ELM performance exceeds the performance of high-order FEM. The ELM method is more efficient than or as efficient as the high-order FEM.

Can artificial neural networks provide a competitive method for scientific computing and in particular for numerical PDEs? Can one devise a neural network-based method for approximating PDEs that can outcompete the traditional numerical techniques? These questions have motivated the current effort and also our recent work in [10]. The ELM type methods developed in [10] and the current work for solving PDEs seek a different approach from the existing DNN-based PDE solvers, in order to achieve high accuracy and competitive computational performance. Our methods attempt to exploit the randomization of a subset of the network weights in order to simplify the the optimization task of the network training, and more importantly we train the neural network by a linear or nonlinear least squares computation (rather than the gradient descent type algorithms). The exponential convergence behavior (for smooth solutions) with respect to the number of training data points and training parameters and the high accuracy exhibited by

these methods are reminiscent of the traditional high-order methods such as the spectral, spectral element or hp-finite element type techniques.

The current work and our recent work in [10] provide strong evidence that the answer to the above questions seems indeed to be positive. Our previous work [10] demonstrates that the ELM type method can be more competitive than or as competitive as the classical second-order FEM. The importance of the current work lies in that it further shows that the ELM type method can be more competitive than or as competitive as the high-order FEM in terms of the accuracy and computational cost. These studies collectively instigate a neural network-based accurate, efficient and competitive technique for numerical approximation of PDEs in computational science and engineering applications.

Acknowledgement

This work was partially supported by NSF (DMS-2012415, DMS-1522537).

References

- [1] P.A. Alaba, S.I. Popoola, L. Olatomiwa, M.B. Akanle, O.S. Ohunakin, E. Adetiba, O.D. Alex, A.A.A. Atayero, and W.M.A.W. Daud. Towards a more efficient and cost-sensitive extreme learning machine: a state-of-the-art review of recent trend. *Neurocomputing*, 350:70–90, 2019.
- [2] A.G. Baydin, B.A. Pearlmutter, A.A. Radul, and J.M. Siskind. Automatic differentiation in machine learning: a survey. *J. Mach. Learn. Res.*, 18:1–43, 2018.
- [3] Z. Cai, J. Chen, M. Liu, and X. Liu. Deep least-squares methods: an unsupervised learning-based numerical method for solving elliptic PDEs. *Journal of Computational Physics*, 420:109707, 2020.
- [4] F. Calabro, G. Fabiani, and C. Siettos. Extreme learning machine collocation for the numerical solution of elliptic PDEs with sharp gradients. *Computer Methods in Applied Mechanics and Engineering*, 387:114188, 2021.
- [5] N.E. Cotter. The stone-weierstrass theorem and its application to neural networks. *IEEE Transactions on Neural Networks*, 4:290–295, 1990.
- [6] R.L. Courant. Variational methods for the solution of problems of equilibrium and vibration. *Bulletin of the American Mathematical Society*, 49:1–23, 1943.
- [7] S. Dong. A convective-like energy-stable open boundary condition for simulations of incompressible flows. *Journal of Computational Physics*, 302:300–328, 2015.
- [8] S. Dong. Multiphase flows of N immiscible incompressible fluids: a reduction-consistent and thermodynamically-consistent formulation and associated algorithm. *Journal of Computational Physics*, 361:1–49, 2018.
- [9] S. Dong and G.E. Karniadakis. P-refinement and p-rethreads. *Computer Methods in Applied Mechanics and Engineering*, 192(19):2191–2201, 2003.
- [10] S. Dong and Z. Li. Local extreme learning machines and domain decomposition for solving linear and nonlinear partial differential equations. *Computer Methods in Applied Mechanics and Engineering*, 387:114129, 2021. (also arXiv:2012.02895).
- [11] S. Dong and Z. Li. A modified batch intrinsic plasticity method for pre-training the random coefficients of extreme learning machines. *Journal of Computational Physics*, 445:110585, 2021. (also arXiv:2103.08042).
- [12] S. Dong and N. Ni. A method for representing periodic functions and enforcing exactly periodic boundary conditions with deep neural networks. *Journal of Computational Physics*, 435:110242, 2021.

- [13] S. Dong and J. Shen. A time-stepping scheme involving constant coefficient matrices for phase field simulations of two-phase incompressible flows with large density ratios. *Journal of Computational Physics*, 231:5788–5804, 2012.
- [14] V. Dwivedi and B. Srinivasan. Physics informed extreme learning machine (pielm) – a rapid method for the numerical solution of partial differential equations. *Neurocomputing*, 391:96–118, 2020.
- [15] W. E and B. Yu. The deep Ritz method: a deep learning-based numerical algorithm for solving variational problems. *Communications in Mathematics and Statistics*, 6:1–12, 2018.
- [16] S.C. Endres, C. Sandrock, and W.W. Focke. A simplicial homology algorithm for Lipschitz optimization. *Journal of Global Optimization*, 72:181–217, 2018.
- [17] G. Fabiani, F. Calabro, L. Russo, and C. Siettos. Numerical solution and bifurcation analysis of nonlinear partial differential equations with extreme learning machines. *Journal of Scientific Computing*, 89:44, 2021.
- [18] A.L. Freire, A.R. Rocha-Neto, and G.A. Barreto. On robust randomized neural networks for regression: a comprehensive review and evaluation. *Neural Computing and Applications*, 32:16931–16950, 2020.
- [19] P.E. Gill, W. Murray, and M.H. Wright. *Numerical Linear Algebra and Optimization*. SIAM, 2021.
- [20] I. Goodfellow, Y. Bengio, and A. Courville. *Deep Learning*. The MIT Press, 2016.
- [21] S. Haykin. *Neural Networks: A Comprehensive Foundation*. Prentice Hall, 1999.
- [22] J. He and J. Xu. MgNet: A unified framework for multigrid and convolutional neural network. *Science China Mathematics*, 62:1331–1354, 2019.
- [23] K. Hornik, M. Stinchcombe, and H. White. Multilayer feedforward networks are universal approximators. *Neural Networks*, 2:359–366, 1989.
- [24] K. Hornik, M. Stinchcombe, and H. White. Universal approximation of an unknown mapping and its derivatives using multilayer feedforward networks. *Neural Networks*, 3:551–560, 1990.
- [25] G. Huang, G.B. Huang, S. Song, and K. You. Trends in extreme learning machines: a review. *Neural Networks*, 61:32–48, 2015.
- [26] G.-B. Huang, Q.-Y. Zhu, and C.-K. Siew. Extreme learning machine: theory and applications. *Neurocomputing*, 70:489–501, 2006.
- [27] G.B. Huang, L. Chen, and C.-K. Siew. Universal approximation using incremental constructive feed-forward networks with random hidden nodes. *IEEE Transactions on Neural Networks*, 17:879–892, 2006.
- [28] A.D. Jagtap, E. Kharazmi, and G.E. Karniadakis. Conservative physics-informed neural networks on discrete domains for conservation laws: applications to forward and inverse problems. *Computer Methods in Applied Mechanics and Engineering*, 365:113028, 2020.
- [29] G.E. Karniadakis, G. Kevrekidis, L. Lu, P. Perdikaris, S. Wang, and L. Yang. Physics-informed machine learning. *Nature Reviews Physics*, 3:422–440, 2021.
- [30] G.E. Karniadakis and S.J. Sherwin. *Spectral/hp element methods for computational fluid dynamics, 2nd edn*. Oxford University Press, 2005.
- [31] E. Kharazmi, Z. Zhang, and G.E. Karniadakis. Variational physics-informed neural networks for solving partial differential equations. *arXiv:1912.00873*, 2019.
- [32] A.S. Krishnapriyan, A. Gholami, S. Zhe, R.M. Kirby, and M.W. Mahoney. Characterizing possible failure modes in physics-informed neural networks. *arXiv:2109.01050*, 2021.

- [33] I.E. Lagaris, A.C. Likas, and D.I. Fotiadis. Artificial neural networks for solving ordinary and partial differential equations. *IEEE Transactions on Neural Networks*, 9:987–1000, 1998.
- [34] I.E. Lagaris, A.C. Likas, and D.G. Papageorgiou. Neural-network methods for boundary value problems with irregular boundaries. *IEEE Transactions on Neural Networks*, 11:1041–1049, 2000.
- [35] H. Lee and I. Kang. Neural algorithms for solving differential equations. *Journal of Computational Physics*, 91:110–117, 1990.
- [36] K. Li, K. Tang, T. Wu, and Q. Liao. D3M: A deep domain decomposition method for partial differential equations. *IEEE Access*, 8:5283–5294, 2020.
- [37] X. Li. Simultaneous approximations of mulvariate functions and their derivatives by neural networks with one hidden layer. *Neurocomputing*, 12:327–343, 1996.
- [38] L. Lin, Z. Yang, and S. Dong. Numerical approximation of incompressible Navier-Stokes equations based on an auxiliary energy variable. *Journal of Computational Physics*, 388:1–22, 2019.
- [39] A.J. Meade and A.A. Fernandez. The numerical solution of linear ordinary differential equations by feedforward neural networks. *Math. Comput. Modeling*, 19(12):1–25, 1994.
- [40] A.J. Meade and A.A. Fernandez. Solution of nonlinear ordinary differential equations by feedforward neural networks. *Math. Comput. Modeling*, 20(9):19–44, 1994.
- [41] S. Panghal and M. Kumar. Optimization free neural network approach for solving ordinary and partial differential equations. *Engineering with Computers*, Early Access, February 2020.
- [42] M. Raissi, P. Perdikaris, and G.E. Karniadakis. Physics-informed neural networks: a deep learning framework for solving forward and inverse problems involving nonlinear partial differential equations. *Journal of Computational Physics*, 378:686–707, 2019.
- [43] K. Rudd and S. Ferrari. A constrained integration (CINT) approach to solving partial differential equations using artificial neural networks. *Neurocomputing*, 155:277–285, 2015.
- [44] E. Samanaiego, C. Anitescu, S. Goswami, V.M. Nguyen-Thanh, H. Guo, K. Hamdia, X. Zhuang, and T. Rabczuk. An energy approach to the solution of partial differential equations in computational mechanics via machine learning: concepts, implementation and applications. *Computer Methods in Applied Mechanics and Engineering*, 362:112790, 2020.
- [45] S. Scardapane and D. Wang. Randomness in neural networks: an overview. *WIREs Data Mining Knowl. Discov.*, 7:e1200, 2017.
- [46] J. Sirignano and K. Spiliopoulos. DGM: A deep learning algorithm for solving partial differential equations. *Journal of Computational Physics*, 375:1339–1364, 2018.
- [47] R. Storn and K. Price. Differential evolution – A simple and efficient heuristic for global optimization over continuous spaces. *Journal of Global Optimization*, 11:341–359, 1997.
- [48] B. Szabo and I. Babushka. *Finite Element Analysis*. John Wiley & Sons, Inc., 1991.
- [49] J. Tang, C. Deng, and G.B. Huang. Extreme learning machine for multilayer perceptron. *IEEE Transactions on neural networks and learning systems*, 32(2):392–404, 2015.
- [50] K. Tang, X. Wan, and Q. Liao. Adaptive deep density estimation for fokker-planck equations. *arXiv:2103.11181*, 2021.
- [51] M.D. Tissera and M.D. McDonnell. Deep extreme learning machines: supervised autoencoding architecture for classification. *Neurocomputing*, 174:42–49, 2016.
- [52] X. Wan and S. Wei. VAE-KRnet and its applications to variational Bayes. *arXiv:2006.16431*, 2020.

- [53] S. Wang, X. Yu, and P. Perdikaris. When and why PINNs fail to train: a neural tangent kernel perspective. *arXiv:2007.14527*, 2020.
- [54] Y. Wang and G. Lin. Efficient deep learning techniques for multiphase flow simulation in heterogeneous porous media. *Journal of Computational Physics*, 401:108968, 2020.
- [55] P.J. Werbos. Beyond regression: new tools for prediction and analysis in the behavioral sciences. *PhD Thesis, Harvard University, Cambridge, MA*, 1974.
- [56] N. Winovich, K. Ramani, and G. Lin. ConvPDE-UQ: Convolutional neural networks with quantified uncertainty for heterogeneous elliptic partial differential equations on varied domains. *Journal of Computational Physics*, 394:263–279, 2019.
- [57] Z. Yang and S. Dong. A roadmap for discretely energy-stable schemes for dissipative systems based on a generalized auxiliary variable with guaranteed positivity. *Journal of Computational Physics*, 404:109121, 2020. (also arXiv:1904.00141).
- [58] R. Yentis and M.E. Zaghoul. VLSI implementation of locally connected neural network for solving partial differential equations. *IEEE Trans. Circuits Syst. I*, 43:687–690, 1996.
- [59] Y. Yu, R.M. Kirby, and G.E. Karniadakis. Spectral element and hp methods. *Encyclopedia of Computational Mechanics, John Wiley and Sons, NY*, 1:1–43, 2017.
- [60] Y. Zang, G. Bao, X. Ye, and H. Zhou. Weak adversarial networks for high-dimensional partial differential equations. *Journal of Computational Physics*, 411:109409, 2020.
- [61] X. Zheng and S. Dong. An eigen-based high-order expansion basis for structured spectral elements. *Journal of Computational Physics*, 230:8573–8602, 2011.